



UNIVERSITÀ
DI TRENTO

DEPARTMENT OF PHYSICS

Master degree in Physics

**Chaotic dynamics of an electronic
implementation of the
Burridge-Knopoff model**

Graduant:

Manuel BITTO

Supervisor:

Leonardo RICCI

Co-supervisor:

Alessio PERINELLI

24 October 2024

Contents

| | |
|--|-----------|
| Introduction | v |
| 1 An electronic analog of the Burridge-Knopoff model | 1 |
| 1.1 Mechanical Burridge-Knopoff model | 1 |
| 1.1.1 Motion of two coupled blocks | 2 |
| 1.1.2 Dimensionless system | 3 |
| 1.2 Electronic analog for the motion of two blocks | 3 |
| 1.3 Characterization of the single block behavior | 4 |
| 1.3.1 Breadboard implementation | 6 |
| 1.3.2 Integrated board implementation | 6 |
| 1.4 Characterization of the double block behavior | 8 |
| 2 Chaos in theory and experiments | 11 |
| 2.1 Dynamical systems | 11 |
| 2.2 Formal definition of chaos | 12 |
| 2.3 The issue of detecting chaos | 12 |
| 2.4 The embedding procedure | 14 |
| 2.4.1 The embedding lattice | 16 |
| 2.5 Maximum Lyapunov exponent | 16 |
| 2.6 Correlation dimension | 19 |
| 2.7 The uniformity region | 20 |
| 2.8 A method for detecting chaos | 21 |
| 2.8.1 Testing the method | 22 |
| 3 Chaos analysis of the electronic Burridge-Knopoff model | 25 |
| 3.1 Two coupled blocks | 25 |
| 3.2 Three coupled blocks | 26 |
| 3.2.1 Block on the boundary | 27 |
| 3.2.2 Block in the center | 28 |
| 3.3 The effects of the oscilloscope quantization | 29 |
| 3.4 Multiple coupled blocks | 32 |
| Appendices | 37 |
| A Chaos analysis for oscilloscope quantization | 39 |

| | |
|--|-----------|
| B Chaos analysis on multiple coupled blocks | 41 |
| Bibliography | 59 |

Introduction

Chapter 1

An electronic analog of the Burridge-Knopoff model

1.1 Mechanical Burridge-Knopoff model

Providing an accurate model of a complex physical system is often a hard, if not impossible, task. One of the most common and interesting situations occurs when a fairly simple model, which perhaps is far cry from the phenomenon behind the system, at least at first sight, actually shows a lot of properties that share very strong analogies with what happens in the real world. One of the most known and important examples of these systems are earthquakes.

The dynamics of earthquakes is highly nonlinear and complex, and not yet fully understood. There are several models that try to simulate the statistical properties of a real earthquake. The most relevant of these properties is the Gutenberg-Richter law [1], a power-law that links the number of observed earthquakes to their magnitude, i.e. the energy released by the earthquake.

One of the models that, when simulated, reproduces these properties fairly well is the Burridge-Knopoff (BK) spring-block model [2], a two-dimensional system of massive blocks lying on a rough horizontal surface. Each block is connected to its nearest neighbors by a set of springs, and linked through another spring to an upper horizontal ceiling moving with constant velocity with respect to the lower plate, as shown in Fig. 1.1.

The blocks are driven by the relative movement of the two rigid plates. When the force on one block reaches some threshold value F_{th} , the block slips, and it is reasonable to assume that the force on that block becomes zero. Then, the force on the four nearest neighbors is increased, often resulting in further slips, and an avalanche can occur.

The purpose of the BK model is the description of the dynamical behavior of real faults, whereby a constant, slow driving motion of plates produces an accumulation of “stress” up to a threshold at which such stress is released through an abrupt motion – i.e. an earthquake – of one or more of the system’s constituent parts.

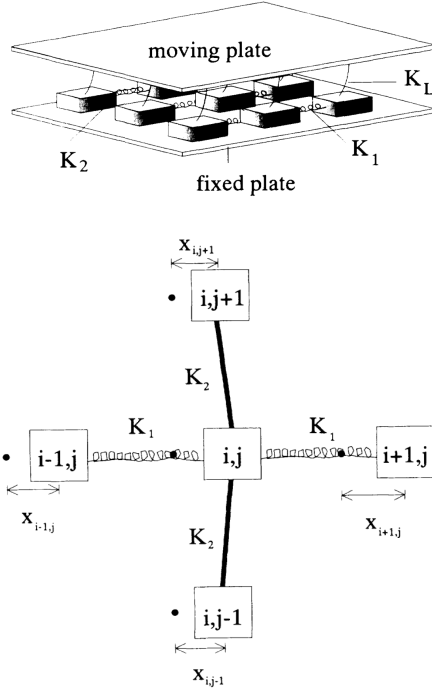


Figure 1.1: Visual representation of the Burridge-Knopoff spring-block model. K_1 and K_2 are the elastic constants, respectively, of the horizontal and vertical springs, while K_L is the elastic constant of the springs connecting the blocks and the moving plate. The figure below represents the interaction between a block and its four nearest neighbors, as a function of the displacement $x_{i,j}$. Figure adapted from Ref. [3].

1.1.1 Motion of two coupled blocks

The mechanical BK model for the motion of two coupled blocks is shown schematically in Fig. 1.2. The upper ceiling moves with respect to the surface with a constant velocity u_d . Let x_1 , x_2 be the displacements of the block positions relative to a state in which the springs are relaxed, and u_1 , u_2 the velocities of the blocks in the lower surface frame, so that $u_i = u_d + \dot{x}_i$ with $i = 1, 2$.

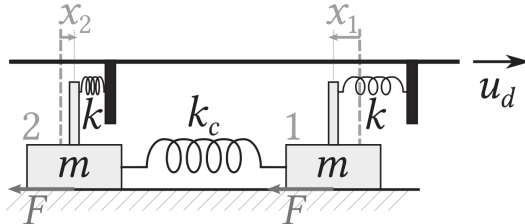


Figure 1.2: Two-blocks mechanical BK model. The upper ceiling, which the blocks are coupled to via springs with elastic constant k , is dragged with constant velocity u_d with respect to the underlying surface. This surface exerts a nonlinear, velocity-dependent friction F to each block's motion. Figure adapted from Ref. [4].

The equations of motion are thus given by

$$\begin{aligned}
m \frac{du_1}{dt} &= -kx_1 - k_c(x_1 - x_2) - F(u_1), \\
\frac{dx_1}{dt} &= u_1 - u_d, \\
m \frac{du_2}{dt} &= -kx_2 - k_c(x_2 - x_1) - F(u_2), \\
\frac{dx_2}{dt} &= u_2 - u_d,
\end{aligned} \tag{1.1}$$

where m is the mass of the blocks, k is the elastic constant of the springs that connect the blocks to the ceiling, k_c is the elastic constant of the spring linking the two blocks, and $F(u)$ is the nonlinear velocity-dependent friction. The velocities are assumed to be non-negative.

1.1.2 Dimensionless system

It is possible to render this system dimensionless by defining the following dimensionless quantities (i takes the values 1 and 2): a time $\tau \equiv t\sqrt{k/m}$, a velocity $\nu_i \equiv u_i/u_0$, a position $\xi_i \equiv x_i\sqrt{k/m}/u_0$, a friction $\varphi(\nu_i) \equiv F(\nu_i)/(u_0\sqrt{mk})$ and a parameter $\lambda \equiv k_c/k$. The four equations of motion can then be written as

$$\begin{aligned}
\frac{d\nu_i}{d\tau} &= -(1 + \lambda)\xi_i + \lambda\xi_{3-i} - \varphi(\nu_i), \\
\frac{d\xi_i}{d\tau} &= \nu_i - \nu_d.
\end{aligned} \tag{1.2}$$

There exists a relative freedom in the choice of the friction $\varphi(\nu)$, provided that (i) $\varphi(\nu < 0) = 0$, (ii) $\varphi(\nu \geq 0) \geq 0$ and (iii) $\varphi(\nu)$ decreases down to zero from a maximum value $\varphi(0)$ that occurs at $\nu = 0$.

It is useful to define the equations of motion also in the case of a lower surface moving with a positive dimensionless velocity $\Delta\nu$, so that $\nu'_i = \nu_i + \Delta\nu$ and $\nu'_d = \nu_d + \Delta\nu$. The system of equations becomes:

$$\begin{aligned}
\frac{d\nu'_i}{d\tau} &= -(1 + \lambda)\xi_i + \lambda\xi_{3-i} - \varphi(\nu'_i - \Delta\nu), \\
\frac{d\xi_i}{d\tau} &= \nu'_i - \nu'_d.
\end{aligned} \tag{1.3}$$

1.2 Electronic analog for the motion of two blocks

In order to analyze the properties of the BK model, it is possible to build an electronic circuit which differential equations are the same as Eqs. 1.3. The first implementation was done by Field, Venturi and Nori [5] by drawing a direct parallelism between mechanical and electrical quantities. The idea was to use capacitance as mass, inductance as the reciprocal of elastic constant, voltage as velocity and current as position.

However, this implementation has two main drawbacks. The first one is the usage of inductances, which are typically bulky and have intrinsically large tolerances compared with other components, resulting in higher uncertainties; moreover, their tunability is very low. The second issue is that the current is a state variable, and it is less straightforward to measure it with respect to voltage.

It is possible to use another implementation [4] which does not rely on inductances and uses only voltages as state variables. In order to do so it is necessary to rewrite the differential equations as integral equations, so that they can be implemented by electronic integrators, which are more stable than the differentiators. The new state variables are defined as $V_i \equiv \nu_i V_0$ and $W_i \equiv \xi_i V_0$ and the new time constant is given by $\tau = RC$, where R and C are suitably chosen resistance and capacitance. Integrating the system of Eqs. 1.3 for a moving surface and replacing $V'_i \equiv V_i + \Delta V$ and $V'_d \equiv V_d + \Delta V$, where $V_d \equiv V_0 \nu_d$ and $\Delta V \equiv V_0 \Delta \nu$, leads to the following system of equations (i takes the values 1 and 2):

$$\begin{aligned} V_i + \Delta V &= -\frac{1}{RC} \int \left[(1 + \lambda) W_i - \lambda W_{3-i} + V_0 \varphi \left(\frac{V_i}{V_0} \right) \right] dt, \\ W_i &= -\frac{1}{RC} \int (V_d - V_i) dt, \end{aligned} \quad (1.4)$$

where $\lambda = R/R_c$ and R_c is a suitably chosen resistance.

These differential equations are implemented by the circuit shown in Fig. 1.3, which makes use of resistors, capacitors, diodes and operational amplifiers, without any inductance. Assuming for a while that ΔV and the nonlinear element $\varphi(V_i/V_0)$ were not present, the two integrations above could be promptly implemented by considering the black part of the circuit diagram.

The nonlinear term is instead represented by the blue part of the diagram and it is implemented as follows. A Schottky diode is inserted on the feedback network on the integrator producing V_i ; this ensures that V_i does not drop below $-V_{\text{diode}}$, where $V_{\text{diode}} \approx 0.3$ V. In order to not contradict the constraint that the “velocity” must be always non-negative, it is necessary to set $\Delta V = V_{\text{diode}}$. In this way the first of the constraints set in Sec. 1.1.2, i.e. $\varphi(V_i < 0) = 0$ is satisfied, since the voltage cannot drop below zero.

The nonlinear friction element consists in a linear drop for the analog of the velocity-weakening force, and it is implemented using two additional op-amps as follows. The output of the first op-amp is given by $V_0 - V_i R_B / R_A$. Downstream of the resistor r , this voltage is prevented to drop below zero by an active clamp made of the second op-amp which has a diode in its feedback network. The resulting voltage is then fed back into the integrator generating V_i through an additional resistor $R - r$.

1.3 Characterization of the single block behavior

With the aim of analyzing the circuit represented in Fig. 1.3, it is necessary to characterize its behavior. The first characterization concerns the function of a single block,

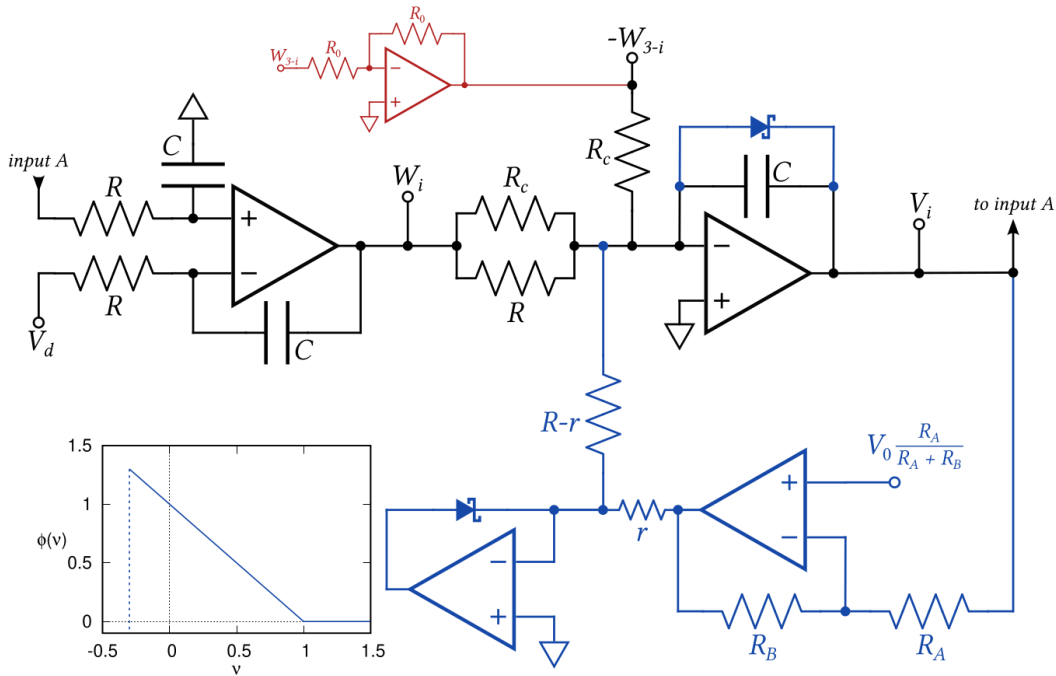


Figure 1.3: Inductorless representation of the BK model. The circuit diagram refers to a single block, labeled by $i = 1, 2$. The bottom left plot shows the characteristic of the nonlinear element, i.e. the blue part of the diagram. The red part is a standard inverting operational amplifier, which is necessary for the coupling between two blocks. Figure adapted from Ref. [4].

in the absence of couplings. In this case $\lambda = 0$ and the differential equations of the system can be simplified as (the subscript i is omitted):

$$\begin{aligned} \frac{d^2V}{dt^2} + \frac{1}{\tau} \varphi' \left(\frac{V}{V_0} \right) \frac{dV}{dt} + \frac{1}{\tau^2} (V - V_d) &= 0, \\ \frac{dW}{dt} &= \frac{1}{\tau} (V - V_d). \end{aligned} \tag{1.5}$$

where φ' is the derivative of the friction with respect to the velocity V . The equation for the velocity is of the kind met in the classical description of stick-slip vibrations [6], i.e. of the self-sustained oscillations induced by friction. This means that an oscillating behavior for V and W has to be expected.

In order to check the validity of these equations, the circuit was physically implemented in two different manners. The first implementation was done on a breadboard using large electronic components; the main issue with this system is that it is not scalable, due to the fact that a single circuit occupies half of the entire space on the breadboard. The second one consists instead in an integrated board in which 25 circuits like the one in Fig. 1.3 were implemented; the scalability issue is solved in this case, so that this board could be utilized to study the behavior of many coupled blocks, as will be done later in this work.

1.3.1 Breadboard implementation

The breadboard implementation was made using 1N5817 Schottky diodes and OP27 op-amps; these op-amps were supplied with $V_{CC} = \pm 12$ V. The nominal values for the resistances and capacitors are $R = R_c = 10 \text{ k}\Omega$, $R_A = R_B = 10 \text{ k}\Omega$, $r = 1.8 \text{ k}\Omega$ and $C = 100 \text{ nF}$, so that the characteristic time of the circuit is $\tau = 1 \text{ ms}$. The input voltages are $V_0 = 1 \text{ V}$ and the variable voltage V_d , while the output voltages are V and W (the subscript i is omitted). A picture of the implementation is shown in Fig. 1.4.

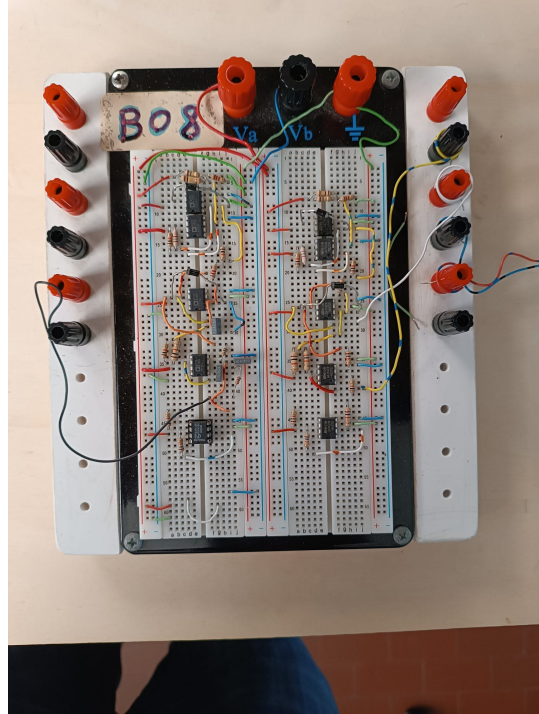


Figure 1.4: Breadboard implementation of two BK blocks, using OP27 op-amps (left) and UA741 op-amps (right).

The single block behavior of this circuit is shown in Fig. 1.5. As expected by Eqs. 1.5, both the velocity V and the position W exhibit an oscillating behavior. While W closely resembles a sinusoidal wave, V possesses a lower clamping that makes it different from a simple wave; this clamping is due to the presence of the Schottky diodes, which prevent that the velocity becomes negative, as discussed in Sec. 1.2. In the end, both the frequency and the amplitude of the waves depend on the driving voltage V_d .

1.3.2 Integrated board implementation

The circuit diagram for each of the 25 chips on the integrated board is equivalent to the one shown in Fig. 1.3. The only differences with the breadboard implementation concern the nonlinear components, i.e. the use of DFLS1100 Schottky diodes and quad operational amplifiers OP470, which should offer comparable performances to the components used in the previous section, i.e. 1N5817 Schottky diodes and OP27

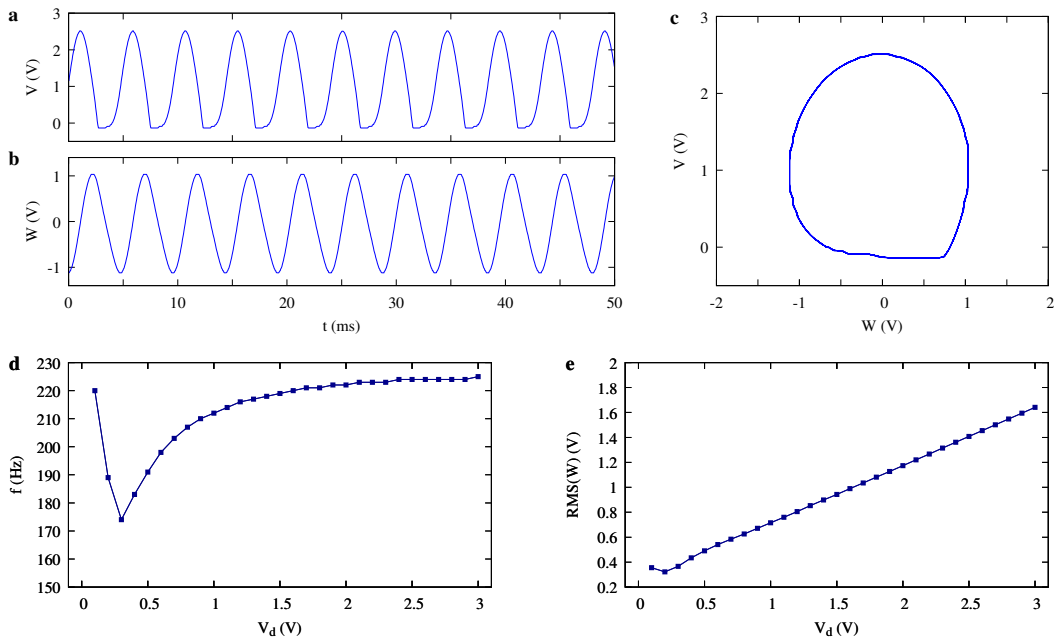


Figure 1.5: Oscillating behavior for the circuit implemented on the breadboard. (a) Plot of W and (b) of V as a function of time, for $V_d = 1$ V. (c) Phase portrait (Lissajous figure) of V vs. W . (d) Frequency and (e) root mean square amplitude of the output signal W as a function of the parameter V_d .

op-amps. A picture of the implementation is shown in Fig. 1.6.

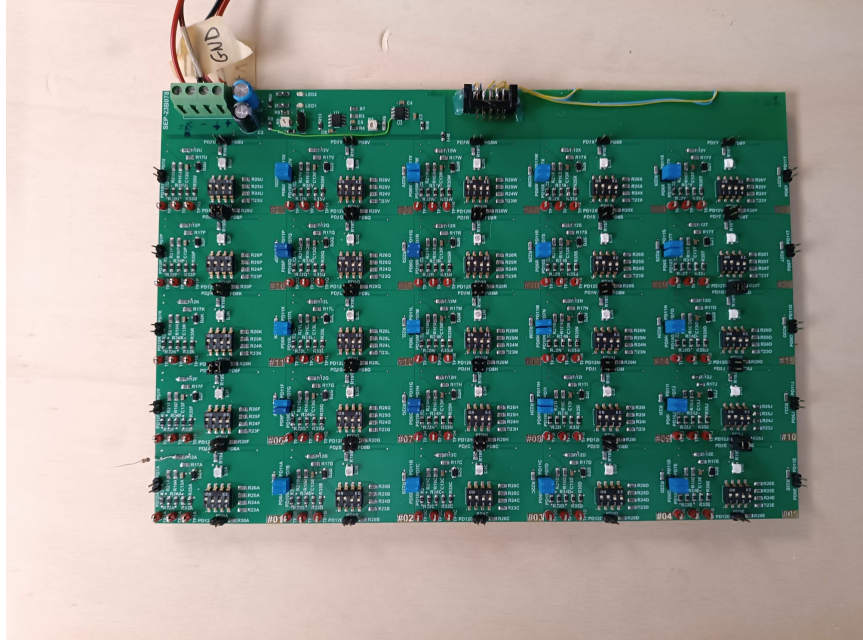


Figure 1.6: Integrated board implementation of 25 BK blocks.

A comparison between the single block behavior of this circuit and the one implemented in the previous section is shown in Fig. 1.7. The most notable difference is the amplitude of the waveforms and of the Lissajous figures, which is higher in the integrated board case. Another discrepancy between the two plots lies in the

frequency behavior at low driving voltage V_d , i.e. the initial “drop” in the frequency is more pronounced in the breadboard case with respect to the integrated circuit. These distinctions are all probably due to the different diodes and op-amps utilized in the two cases, but they do not modify the actual dynamics of the circuit.

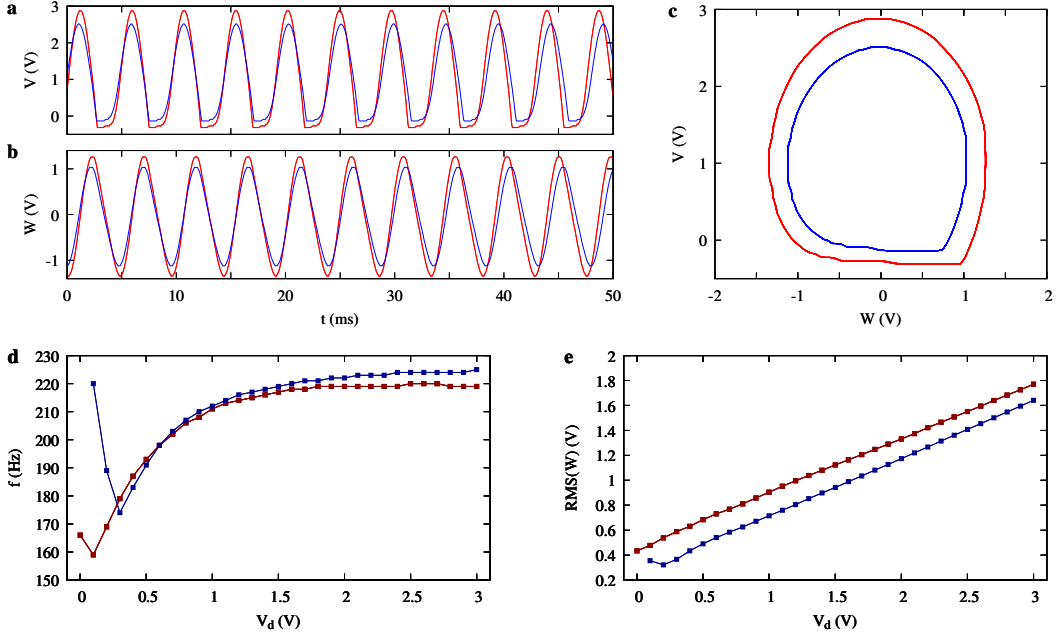


Figure 1.7: Oscillating behavior for the circuit implemented on the integrated board (red) and the one implemented on the breadboard (blue). (a) Plot of W and (b) of V as a function of time, for $V_d = 1$ V. (c) Phase portrait (Lissajous figure) of V vs. W . (d) Frequency and (e) root mean square amplitude of the output signal W as a function of the parameter V_d .

Despite being slightly different, both implementations comply with the oscillating behavior predicted by Eqs. 1.5. It is thus reasonable to assume that both the integrated circuit and the one on the breadboard can potentially be a consistent physical implementation of the BK model. In order to furtherly strengthen this hypothesis, an analysis on the behavior of two coupled blocks will be carried out in the next section. From now on, only the integrated board implementation will be considered, due to the scalability issues that were discussed beforehand.

1.4 Characterization of the double block behavior

The coupling between two blocks is performed by connecting the inverted voltage $-W_2$ of the second block to the inverting input of the op-amp generating V_1 on the first block (see Fig. 1.3), and viceversa, in order to comply with Eqs. 1.4.

The behavior of the two coupled blocks is shown in Fig. 1.8. By looking at the waveforms $V_i(t)$ and $W_i(t)$ it is possible to notice that the simple periodic behavior is no longer observed. Furthermore, the Lissajous figures do not show a stationary orbit like the single block case. This hints that the dynamics in the presence of coupling might be chaotic, i.e. deterministic but unpredictable, and surely non-periodic.

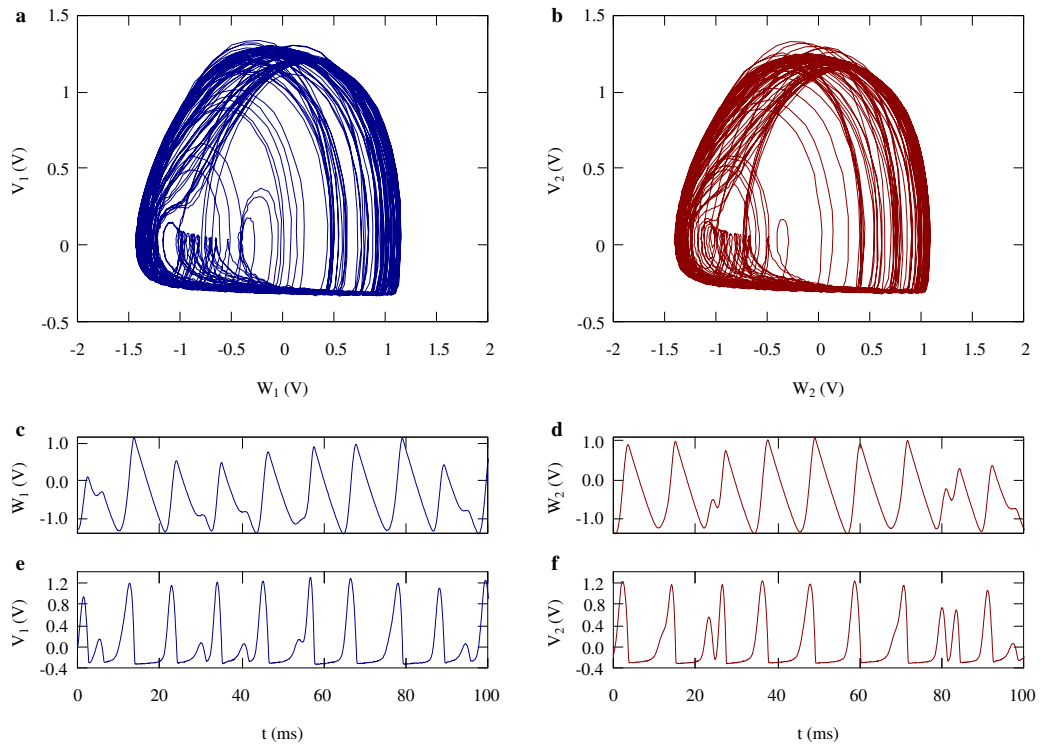


Figure 1.8: Seemingly chaotic behavior of two coupled blocks for $V_d = 0.05$ V. Phase portraits of V_i vs W_i for the first (a) and second (b) block, for a total time of 1 s. Time series plots for W_1 (c), V_1 (e), W_2 (d) and V_2 (f), for a total time of 100 ms.

Another way to check the presence of chaos in the system is to make use of a bifurcation diagram, i.e. the distribution of the local maxima of a state variable (position, velocity) as a function of an external parameter (driving force). This diagram is shown in Fig. 1.9 for the position W_1 (W_2 behaves similarly) as a function of V_d .

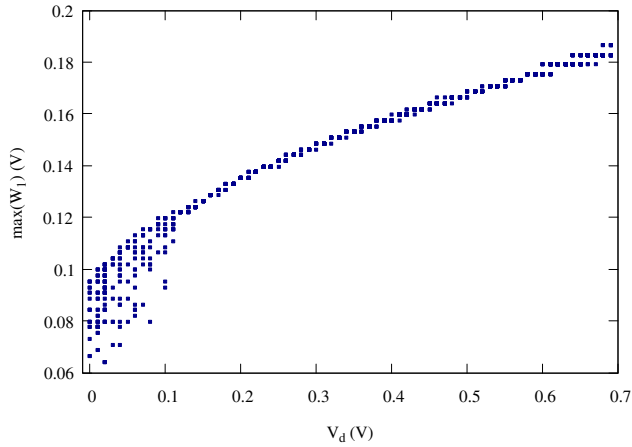


Figure 1.9: Bifurcation diagram for two coupled blocks. The local maxima of W_1 are plotted as a function of the external parameter V_d , which is varied in steps of 10 mV.

The scan of the V_d parameter was carried out by switching off the circuit's power supply, changing the voltage V_d , and then switching the power supply back on. This

ensured that the recorded evolution was independent of the previous state. It is possible to notice that the dynamics is richer for $V_d \lesssim 0.11$ V, where several maxima can be detected. In contrast, for $V_d \gtrsim 0.11$ V, only one maximum can be observed; in this regime the system behaves similarly to the single block case, manifesting periodic sinusoidal-like oscillations.

It is therefore safe to assume that, for low driving voltages V_d , the coupled system of two blocks shows a chaotic behavior. The reason why this does not occur at higher voltages might be that the driving force is so strong that the blocks behave independently of it. Nonetheless, these analyses are not enough to say that this circuit is actually a chaotic system. In Chapter 2 the mathematical conditions that characterize a chaotic system are defined; making use of those, a method that establishes whether an experimental system is chaotic or not is presented.

Chapter 2

Chaos in theory and experiments

2.1 Dynamical systems

The concept of dynamical systems is quite general, since anything that moves can be considered as a dynamical system [7]. If these changes are driven by specific rules, we say that the system is deterministic; otherwise, if the rules are random, it is stochastic. The main feature of chaotic systems is the fact that they are unpredictable despite being deterministic; in order to better explain the meaning of this statement, it is essential to involve some mathematical definitions.

The instantaneous state of a dynamical system is described by a vector \mathbf{s} within a state space \mathcal{S} (typically, $\mathcal{S} \subseteq \mathbb{R}^M$). The state vector evolves in time according to an evolution operator \mathcal{E}_t such that:

$$\mathbf{s}(t + t_0) = \mathcal{E}_t[\mathbf{s}(t_0)]. \quad (2.1)$$

In theoretical systems the state space \mathcal{S} is well-defined and the evolution operator \mathcal{E}_t is given; in most cases, \mathcal{E}_t is defined by a set of differential equations which can be solved, analytically or numerically, to find the system's evolution $\mathbf{s}(t)$ out of the initial conditions $\mathbf{s}(0)$.

A dynamical system is defined to be linear if the superposition principle holds, i.e.:

$$\mathcal{E}_t[c_1\mathbf{s}_1 + c_2\mathbf{s}_2] = c_1\mathcal{E}_t[\mathbf{s}_1] + c_2\mathcal{E}_t[\mathbf{s}_2]. \quad (2.2)$$

If the last equality is not satisfied the system is said to be nonlinear. Nonlinearity is a necessary (but not sufficient) condition for the system to be chaotic.

In experimentally observed systems the state space is not always fully accessible; moreover, the evolution operator \mathcal{E}_t is rarely known. Observing a system consists in recording some signal $y(t)$ out of it through some measurement function \mathcal{M} acting on the system's state, i.e. $y(t) = \mathcal{M}[\mathbf{s}(t)]$. This continuous signal is always sampled and digitized, producing a finite time series (or sequence) $\{y_n\}$ with $n = 1, \dots, \ell$.

2.2 Formal definition of chaos

An universally accepted mathematical definition of chaos does not exists but a commonly used definition is the following, originally formulated by Robert Devaney [8].

Three conditions are necessary and sufficient to define a system as chaotic: (i) sensitivity to initial conditions; (ii) topological transitivity; (iii) density of periodic orbits.

Going into detail:

- (i) Sensitivity to initial conditions is a property that characterizes chaotic systems and makes their evolution hard to predict.

Given two initial conditions $\mathbf{s}_1(0)$, $\mathbf{s}_2(0)$ that are arbitrarily close within the state space ($\|\mathbf{s}_1(0) - \mathbf{s}_2(0)\| < \varepsilon$ for every $\varepsilon > 0$), the system having sensitive dependence on initial conditions means that the two trajectories evolving out of these initial conditions diverge exponentially in time, i.e. for large t :

$$\|\mathbf{s}_1(t) - \mathbf{s}_2(t)\| \propto e^{\lambda t}, \quad (2.3)$$

where λ is called maximum Lyapunov exponent (MLE). In order for the system to be chaotic, λ has to be positive.

It is also important that the orbits $\mathbf{s}_1(t)$, $\mathbf{s}_2(t)$ remain bounded at large t , otherwise, if orbits went to infinity, it would be simple for their distance to diverge exponentially.

The most important consequence of this property is that, as far as we are able to precisely measure the initial state of a system, there will always be a small error (given for example by measuring instruments) which can grow rapidly over time. Therefore, even if we know exactly the deterministic laws governing time evolution, our predictions on the behaviour of the system after a certain time will no longer be reliable. Furthermore, if the precision with which we measure the state of the system in the initial instant is improved by a factor of 10, we only gain a $\log(10)$ factor for the maximum time for which the predictions are accurate.

- (ii) Topological transitivity is the property according to which a chaotic trajectory eventually connects any region of the state space with any other. In other words, the state space of a chaotic system cannot be decomposed into disjoint subsets.
- (iii) Density of periodic orbits means that for any given point in the state space there is a periodic orbit that passes arbitrarily close to it, i.e. periodic orbits make up a dense set.

2.3 The issue of detecting chaos

When dealing with experimentally observed systems, the precise laws that describe the dynamics are unknown. What is known is the time series, which can be used

to assess condition (i) of Devaney's definition of chaos. Instead, conditions (ii) and (iii) are difficult to identify with the time series only. However, there are observable consequences. In particular, the time evolution of a chaotic system in the state space always converges to an object called strange attractor, characterized by a fractal structure [7, 9]. An example can be seen in Fig. 2.1. Strange attractors exhibit self-similarity (or self-affinity¹) and have a non-integer dimensionality.

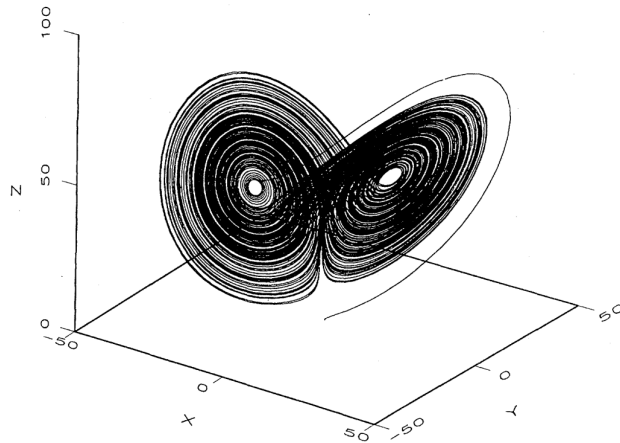


Figure 2.1: Lorenz attractor [11] in three-dimensional phase space $(x(t), y(t), z(t))$. Figure adapted from Ref. [12].

To understand what it means to have non-integer dimensionality, suppose to consider a fractal object with dimension $1 < D < 2$. We know in general that if we have an object of dimension D (assuming that it has a mass density), taking an arbitrary point in it and considering an open ball centered in that point, we can measure the mass contained in the ball as a function of the radius. For small distances $m(r) \propto r^D$. For the same density and radius, the fractal "weighs" more than a line but less than a surface, as if a dense set (which is the set of the periodic orbits) had been removed from the surface.

Self-similarity, instead, is the exhibition of similar patterns at increasingly smaller scales; in other words, a fractal does not appear simplified when we see it zoomed, as can be seen in Fig. 2.2. Despite strange attractors also existing in non-chaotic systems [13], the estimate of the system's non-integer dimension is often used as a tool to identify chaos.

Another important property allows us to identify chaos: the trajectory winds around forever never repeating on a strange attractor and the time series arising by chaotic systems are aperiodic and characterized by broad, noise-like Fourier spectra, as can be seen in Fig. 2.3. This also means that linear techniques such as fast Fourier transform (FFT) applied to sequences cannot distinguish between a chaotic system and a stochastic one, e.g. a Gaussian white noise source (GWN).

One more necessary requirement to sustain a chaotic flow is that the number of

¹In general, it is more correct to speak of self-affinity, since in the case of self-similarity the object is scaled by the same amount in all space directions, but in self-affinity scaling is not necessarily identical in all directions [10].

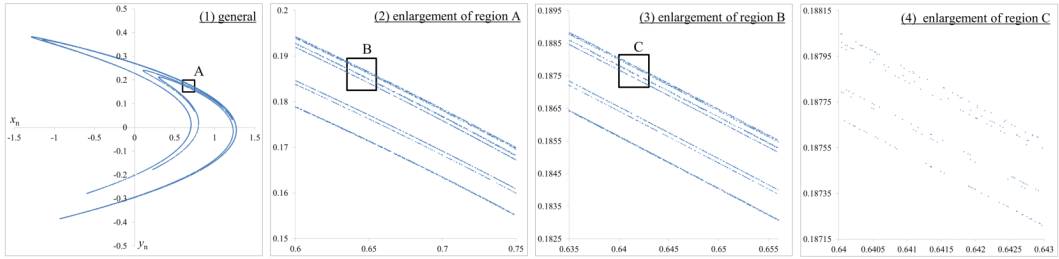


Figure 2.2: Self-similarity of the Hénon attractor: at all magnification levels the same qualitative structures are visible. Figure adapted from Ref. [14].

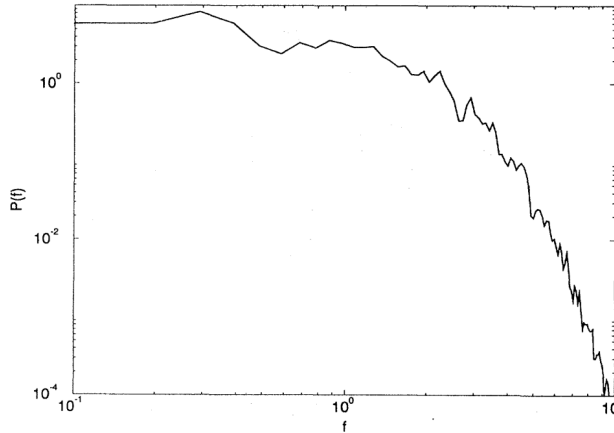


Figure 2.3: Power spectrum of the Lorenz system [11]. Figure adapted from Ref. [12].

independent dimensions has to be at least three, assuming no discontinuities [15]; this is due to the fact that with two or less independent variables the trajectory will eventually intersect itself, which cannot happen due to the aperiodic nature of chaotic dynamics.

2.4 The embedding procedure

In experimentally observed systems it is only possible to utilize the finite time series $\{y_n\}$, with the aim to at least obtain some invariant quantities, e.g. the maximum Lyapunov exponent or the “effective” dimension of the system. Under certain conditions, a procedure exists with which it is possible to reconstruct the entire state space using only one variable, which is a function of the state space vector $\mathbf{s}(t)$. This procedure is called “time delay embedding” [16].

Embedding consists in building a sequence of m -dimensional vectors \mathbf{Y}_n by picking m time-delayed samples of the sequence y_n , i.e.:

$$\mathbf{Y}_n = (y_n, y_{n+L}, y_{n+2L}, \dots, y_{n+(m-1)L}), \quad (2.4)$$

where the parameter L is an integer number and is called “lag”. It is perfectly equivalent to make use of a “causal” version of Eq. 2.4 in which the chosen samples are y_{n-kL} instead of y_{n+kL} , with $k = 0, \dots, m - 1$ [17].

An example of embedding can be seen in Fig. 2.4. This procedure maps the

time series into a “reconstructed space” in which the trajectory somehow resembles a strange attractor.

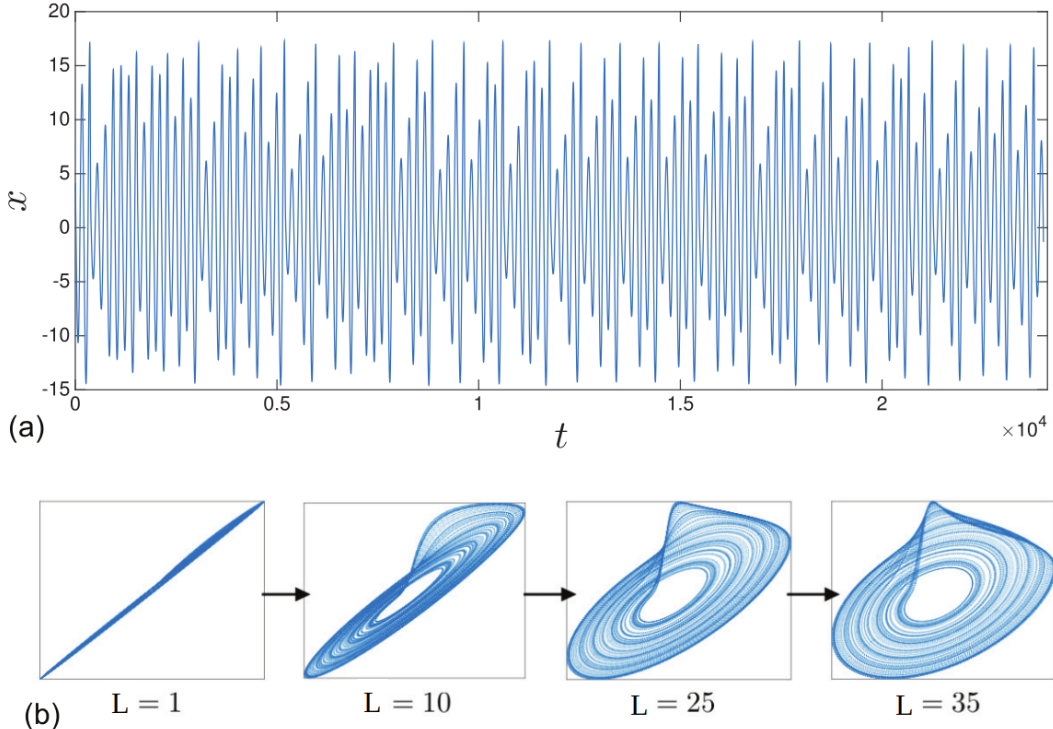


Figure 2.4: (a) A time series from the Rössler system [18] and (b) a number of delay-coordinate embeddings of that time series with different values of the lag L . Figure adapted from Ref. [17].

It has in fact been proven by Takens [19] and Mañé [20] that if the parameters m (dimension) and L (lag) are suitably chosen, the reconstructed state space evolution is topologically identical to the actual state space dynamics. This means that a “good” embedding provides a smooth one-to-one map from the original state space evolution to the reconstructed one, therefore enabling us to estimate the properties of the original system that are invariant under this mapping.

The two conditions under which Takens’ theorem holds regard the embedding parameters (m, L) . The first one requires that $m > 2D$, where D is the dimension of the manifold corresponding to the time evolution of the system, which is not known a priori; this condition can be relaxed to $m > D$ if estimating correlation dimension [21]. The second one states that L must not be a multiple of the period of any system’s orbit [22].

Aside from these two minimal conditions, since Takens’ theorem is an existence theorem, it does not give any hint on how to find the best embedding parameters. The reason for this is that as long as the two conditions are met, every choice for the pair (m, L) is good for reconstructing the dynamics; however, this is valid only for noiseless, finely sampled and infinitely long sequences. In reality, the issue of optimal embedding is a very active field in the physics of chaos, and several techniques have been developed in order to overcome this problem [23, 24, 25].

Considering the dimension m , choosing $m \gg 1$ ensures, in principle, that m is greater than $2D$. However, if m is too large the directions orthogonal to the deterministic noiseless trajectory will be dominated by noise and will not provide extra information; in other words, supposing that m_0 is the minimum dimension for which the system is correctly embedded, the remaining $m - m_0$ dimensions would be populated by noise, being thus redundant and resulting in an increase of the computational cost. Moreover, the larger is the embedding dimension m , the fewer independent embedding vectors are available, which is an issue considering the finiteness of the time series.

The choice on the lag L is also not trivial. If L is too short, the elements of the embedding vectors \mathbf{Y}_n will be strongly correlated, resulting in all the points being clustered on the diagonal of the reconstructed space (see Fig. 2.4b); in presence of noise, therefore, the trajectory would be indistinguishable from the diagonal itself. On the other hand, a too large L presents the opposite problem, i.e. the elements of \mathbf{Y}_n to be completely uncorrelated with each other; this implies that the time evolution is “blurred”, in the sense that the trajectory is folded over on itself and the system evolution is lost.

2.4.1 The embedding lattice

Since a single optimal choice for (m, L) does not necessarily exist, the embedding of the sequence can be carried out for several values of the embedding parameters, considering that many values for the pair (m, L) can provide reconstructions of the underlying dynamics that are equivalently good. More specifically, the procedure is carried out for each element of an embedding lattice, i.e. $\{(m, L) | m \in [2, m_{\max}], L \in [1, L_{\max}]\}$.

Suitable embedding choices are expected to comply with two requirements concerning the corresponding embedding window $w = (m - 1)LT$, which corresponds to the time span covered by each embedding vector (T is the sampling time of the sequence). On the one hand, the embedding window has to be larger than the redundancy time τ_R , so that the points in the reconstructed space are not too close to the diagonal. On the other hand, the embedding window has to be smaller than the irrelevance time τ_I , after which the points are causally disconnected and the noise overcomes the dynamics.

The above requirements can then be expressed as $\tau_R/T \lesssim w \lesssim \tau_I/T$. In the embedding lattice, each window w identifies a hyperbola. Therefore, the irrelevance and redundancy times correspond to two hyperbolae within the embedding lattice, and the region bounded by them is where suitable embedding choices can be expected.

2.5 Maximum Lyapunov exponent

It is now important to formally define the invariant quantities that will be used to decide if an experimentally observed system is chaotic or not, the first one being the maximum Lyapunov exponent (MLE) [12, 26]. There are as many Lyapunov

exponents as the number of state space dimensions: each exponent λ_i corresponds to one of the independent directions along which fiducial volumes within the state space contract ($\lambda_i < 0$) or expand ($\lambda_i > 0$) in an infinitesimal time interval. The MLE λ_1 is the most relevant of the spectrum, since its sign establishes whether the system stabilizes on a fixed point ($\lambda_1 < 0$), stabilizes on a limit cycle ($\lambda_1 = 0$) or is unstable ($\lambda_1 > 0$). A positive MLE is the main hallmark of chaos.

The qualitative behavior of the Lyapunov exponents is shown in Fig. 2.5. In these figures three kinds of phase-space behaviour are displayed. In Fig. 2.5a an exponential divergence of two nearby points on different orbits in the attractor is shown. This chaotic motion is characterised by a positive Lyapunov exponent. In Fig. 2.5b the behaviour of nearby points on the same orbit in the attractor is shown. The separation of these points neither grows nor shrinks exponentially fast so the associated Lyapunov exponent is zero. Finally, in Fig. 2.5c, the decay of a transient or perturbation to the attractor is illustrated. The associated exponent is negative.

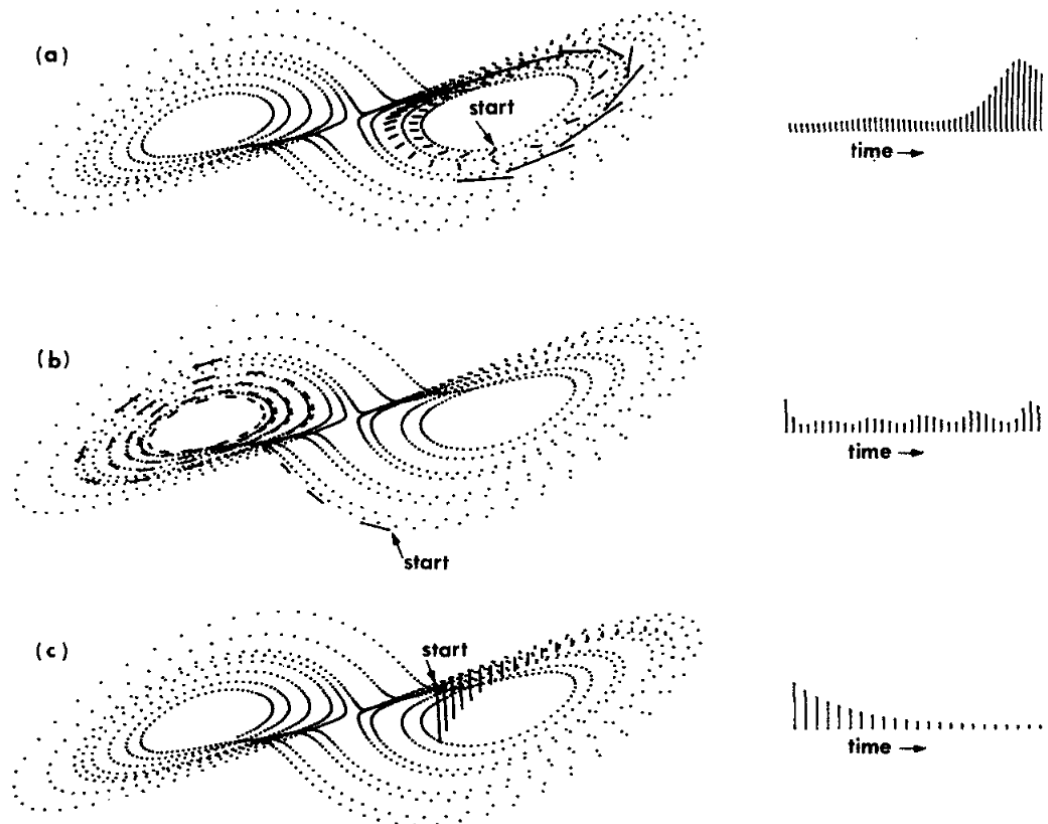


Figure 2.5: Short-term evolution of the separation vector between three pairs of nearby points for the Lorenz attractor [11]. The true magnitude of the evolving vector appears to the right of each figure, (a) An expanding direction ($\lambda_1 > 0$). (b) A slower than exponential direction ($\lambda_2 = 0$). (c) A contracting direction ($\lambda_3 < 0$). Figure adapted from Ref. [26].

It is possible to estimate the MLE through the embedded sequence by making use of the so-called divergence rate method [27]. This method is based on the evaluation of the time-dependent divergence exponent $\Lambda(k)$, which quantifies the average separation

of nearby trajectories. The estimation of this exponent is done by selecting random pairs (i, j) of neighboring vectors in the embedded sequence $\{\mathbf{Y}_n\}$, i.e. such that $\|\mathbf{Y}_i - \mathbf{Y}_j\| < r$, where r is some “shell radius”; the divergence exponent is then calculated as:

$$\Lambda^{m,L}(k) = \frac{1}{N_{\text{pairs}}} \sum_{i,j} \log \left(\frac{\|\mathbf{Y}_{i+k} - \mathbf{Y}_{j+k}\|}{\|\mathbf{Y}_i - \mathbf{Y}_j\|} \right), \quad (2.5)$$

where the superscript m,L indicates once again the dependence on the embedding parameters.

The time-dependent divergence exponent measures the progressive separation, as a function of the time delay k , of the trajectories corresponding to initially close points $\mathbf{Y}_i, \mathbf{Y}_j$. The initial proximity of the vector pairs is tuned by changing the shell radius r , which is typically estimated as the distance corresponding to the a given percentile p of the sample distribution of all Euclidean distances [28, 29].

A source of error regarding the estimation of the MLE are temporal correlations within the input sequence. This issue can be avoided by selecting pairs of points that are distant in time more than some delay c_0 , i.e. constraining $|i - j| \geq c_0$. Typically, c_0 is chosen to be the first zero of the autocorrelation function [30] or its first minimum [31].

If the underlying system is chaotic, $\Lambda(k)$ is expected to grow linearly with k , as a result of the exponentially increasing numerator within the logarithm of Eq. 2.5. Suitably fitting this linear growth provides the value of the MLE. The growth of $\Lambda(k)$ cannot continue for arbitrarily large values of k : eventually, the separation becomes comparable to the size of the attractor and the divergence exponent saturates. This can be seen in Fig. 2.6.

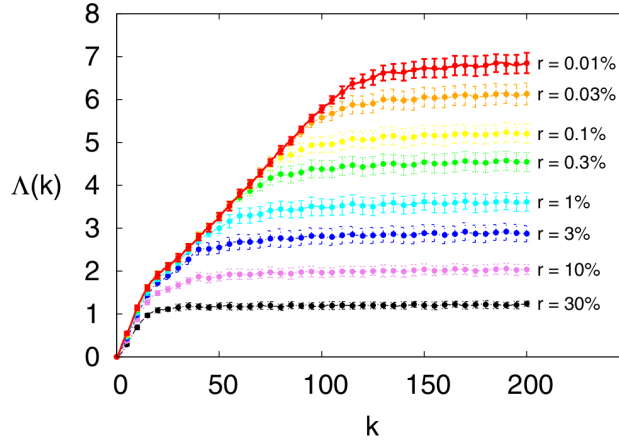


Figure 2.6: Time-dependent divergence exponent $\Lambda(k)$ for the Lorenz attractor [11], obtained by using the embedding pair $(3, 3)$. The different plots correspond to eight different values of r : 0.01%, 0.03%, 0.1%, 0.3%, 1%, 3%, 10%, and 30%. For the sake of clarity, only one point every five is plotted. Figure adapted from Ref. [28].

2.6 Correlation dimension

The second fundamental invariant quantity that characterizes a chaotic system is the correlation dimension [12]. The simplest definition of dimension is the (integer) number of coordinates that are needed to specify a state, e.g. the number of differential equations of a system. This is geometrically related to the concept of how (hyper) volumes scale as a function of a characteristic length parameter. One way to estimate the dimension of a set of points is the box-counting method, which consists in partitioning the space in hypercubes of size l and by counting, as a function of l , the fraction $\eta(l)$ of these hypercubes containing at least one point of the set. The dimension can then be calculated using the fact that $\eta(l \rightarrow 0) \propto l^D$. Since this method is very sensitive and computationally demanding [32], it is useful to search for other ways to estimate the dimension.

Given a set of points $\{\mathbf{Y}_n\}$ within an m -dimensional space partitioned in hypercubes of size l , and given p_i the fraction of points of the set that fall within the i -th hypercube, the generalized dimension is defined as [7]:

$$D_q = \lim_{l \rightarrow 0} \frac{1}{q-1} \frac{\log(\sum_i p_i^q)}{\log l}. \quad (2.6)$$

This definition provides a whole spectrum of invariant quantities for $-\infty < q < \infty$. For example, D_0 is exactly the dimension calculated with the box-counting method, i.e.:

$$D_0 = \lim_{l \rightarrow 0} \frac{\log(\sum_i 1)}{\log l} = \lim_{l \rightarrow 0} \frac{\log \eta(l)}{\log l}. \quad (2.7)$$

The dimension for $q \rightarrow 1$ can instead be calculated using L'Hospital's rule, resulting in:

$$D_1 = \lim_{l \rightarrow 0} \frac{\sum_i p_i \log p_i}{\log l}. \quad (2.8)$$

D_1 is called informational dimension [12] due to the numerator being related to information entropy. In a uniform fractal, in which $p_i = 1/N$ for every i , $D_1 = D_0$; instead, if the p_i are different, $D_1 < D_0$. This is true in general for every q , namely $D_i \leq D_j$ if $i > j$, when the equality only holds in a uniform fractal.

Finally, one of the most utilized dimensions in chaos theory is the correlation dimension, defined as:

$$D_2 = \lim_{l \rightarrow 0} \frac{\log(\sum_i p_i^2)}{\log l}. \quad (2.9)$$

The numerator constitutes a two-point correlation function, measuring the probability of finding a pair of random points within a given partition element, just as the numerator in the definition of D_1 measures the probability of finding one point in a given element.

The reason why correlation dimension is so utilized lies in the fact that there is a very efficient way to estimate it, observed by Grassberger and Procaccia [33]. Due to the exponential divergence of the trajectories, most pairs $(\mathbf{Y}_i, \mathbf{Y}_j)$ with $i \neq j$ will be dynamically uncorrelated pairs of essentially random points. The points lie however

on the attractor, therefore they will be spatially correlated. This spatial correlation can be measured with the correlation integral $C(r)$, defined as:

$$C(r) = \lim_{\ell \rightarrow \infty} \frac{1}{\ell^2} \times \{\text{number of pairs } (i, j) \text{ whose distance is less than } r\}, \quad (2.10)$$

where ℓ is the total number of points in the reconstructed space. Grassberger and Procaccia proved that for small distances the correlation integral grows as $C(r) \propto r^{D_2}$. It is thus possible to estimate the correlation dimension by extracting random pairs of vectors in the embedded sequence, evaluating then a “sample” version of Eq. 2.10, namely:

$$C^{m,L}(r) = \frac{1}{N_{\text{pairs}}} \sum_{i,j} \theta(r - \|\mathbf{Y}_i - \mathbf{Y}_j\|), \quad (2.11)$$

where $\theta(x)$ is the Heaviside function and the superscript m,L indicates the dependence of this sample correlation integral on the embedding parameters.

Like in Section 2.5, it is important that the time separation between the pairs (i, j) is greater than the autocorrelation time, i.e. $|i - j| \geq c_0$ [30, 31]. Ignoring this issue can lead to underestimates of the dimension D_2 [30] or spurious contributions even in the case of stochastic sequences [34].

Another efficient manner to estimate the correlation dimension makes use of the divergence exponent $\Lambda(k)$. As was already discussed in Section 2.5, if $\Lambda(k)$ exhibits a linear behavior it is possible to estimate the MLE as the slope of the curve. For sufficiently large values of k , the divergence exponent $\Lambda(k)$ reaches a saturation value Λ_{pl} , referred to as a “plateau” (see Fig. 2.6). In the case of a chaotic source of finite correlation dimension ν , the plateau turns out to linearly depend on the logarithm of the percentile p [24]:

$$\Lambda_{\text{pl}} = \Lambda' - \frac{1}{\nu} \log p, \quad (2.12)$$

where Λ' is a constant that depends on the embedding parameters. This dependence can thus be exploited to estimate the sample correlation dimension ν out of an input scalar sequence by carrying out a linear fit on a set of $(\log p, \Lambda_{\text{pl}})$ data points.

2.7 The uniformity region

It is now possible to define a criterion that establishes whether an embedding pair (m, L) correctly reconstructs the state space or not. A possible approach consists in searching for a so-called “uniformity region” in the embedding lattice [24], i.e. a region in which the correlation dimension ν does not change significantly.

If a system having dimension D is embedded with $m < D$, the full dimensionality of the system cannot be unfolded and the embedded sequence simply fills all the available space. Consequently, for any $m < D$, correlation integrals exhibit a scaling $\propto r^m$, rather than $\propto r^D$. On the other hand, for $m > D$ and regardless of m , the correct scaling $\propto r^D$ holds in principle; in reality, due to the presence of noise, which has infinite correlation dimension, the scaling will be $\propto r^m$ also in the case of too large m values.

This statement can also be interpreted in the following way. If the embedding window w is too small or too large, the estimated correlation dimension ν will be different from the actual dimension of the system; however, there exists an intermediate region in which ν is the correct correlation dimension, thus ν will be practically constant in the entirety of this region. This uniformity region is the one in which the embedding window lays between the redundancy time τ_R and the irrelevance time τ_I .

2.8 A method for detecting chaos

The most utilized tools for detecting chaos, namely the embedding lattice, the maximum Lyapunov exponent and the correlation dimension, have now been introduced. It is thus possible to establish an efficient procedure which not only searches for the best embedding parameters (m, L) , but also provides estimates for the invariant quantities that characterize chaos [24].

- The scalar sequence $\{y_n\}$ is obtained by sampling the signal $y(t)$ with a sampling time T ; the time series is then supposed to be standardized as $y \rightarrow (y - \bar{y})/\bar{\sigma}$, where \bar{y} and $\bar{\sigma}$ are the sequence's sample mean and sample standard deviation, respectively.
- The maximum values for the embedding dimension m and lag L are chosen, so that the embedding lattice $\{(m, L) | m \in [2, m_{\max}], L \in [1, L_{\max}]\}$ is well defined.
- For each value of (m, L) the divergence exponent $\Lambda^{m,L}(k)$ is calculated with the methods discussed in Section 2.5, and for different values of the percentile p . An important step in the algorithm is that, rather than considering a single calculation for each value of k , each point of $\Lambda^{m,L}(k)$ and the respective uncertainty $\sigma_{\Lambda^{m,L}}(k)$ is determined as the pointwise sample mean and sample standard deviation of a set of N_Λ different calculations, respectively:

$$\begin{aligned}\Lambda^{m,L}(k) &= \frac{1}{N_\Lambda} \sum_{i=1}^{N_\Lambda} \Lambda_i^{m,L}(k), \\ \sigma_{\Lambda^{m,L}}(k) &= \sqrt{\frac{1}{N_\Lambda - 1} \sum_{i=1}^{N_\Lambda} [\Lambda_i^{m,L}(k) - \Lambda^{m,L}(k)]^2}.\end{aligned}\tag{2.13}$$

- As was discussed in Section 2.6, the divergence exponent reaches a plateau $\Lambda_{\text{pl}}^{m,L}$ for large values of k , namely:

$$\Lambda_{\text{pl}}^{m,L}(p) = \lim_{k \rightarrow \infty} \Lambda^{m,L}(k)\tag{2.14}$$

where the dependence on the percentile p is retained. Collecting the plateau value for each percentile p , it is possible to fit Eq. 2.12 in order to easily estimate the correlation dimension ν .

- If the procedure was carried out correctly, at this point there is an estimate of ν for each value of the embedding pair (m, L) . If a uniformity region is present, the system is most likely a chaotic system.

- In the end, it is possible to evaluate the maximum Lyapunov exponent for the embedding pairs in the uniformity region, by simply calculating the slope of the divergence exponent for small values of k . Averaging these values of the MLE can lead to an estimate of the actual MLE of the system.

The strength of this procedure comes from the fact that both the correlation dimension and the maximum Lyapunov exponent can be calculated from the divergence exponent. Moreover, with this method several values of the embedding parameters can be deemed as valid.

2.8.1 Testing the method

In order to test if this approach actually works, this method has been tested on many of the most common chaotic systems [24]. A prototypical example can be the Lorenz system [11], a three-dimensional chaotic system which differential equations are:

$$\begin{aligned}\dot{x} &= \sigma(y - x), \\ \dot{y} &= x(r - z) - y, \\ \dot{z} &= xy - bz,\end{aligned}\tag{2.15}$$

where the parameters are set as $\sigma = 10$, $r = 28$ and $b = 8/3$.

Upon randomly setting the starting point, the differential equations were integrated via a Runge-Kutta Prince-Dormand algorithm [35] with integration step $dt = 0.03$, which is also taken as the sampling time T . The sequence to analyze corresponds to 10^5 samples of the x coordinate of the system.

The embedding lattice was set as $m \in [2, 20]$ and $L \in [1, 20]$. The correlation dimension for each value of the embedding pair is shown in Fig. 2.7. A uniformity region can be identified around $\nu \simeq 2.05$. In order to improve this estimate, the joint distribution, i.e. the correlation dimension as a function of the embedding window, is shown in Fig. 2.8. Here the uniformity region is more visible, providing estimates for τ_R and τ_I , as well as improving the evaluation of the correlation dimension, which now yields $\nu = 2.051 \pm 0.008$. This value is in agreement with conventional assessments made by applying the standard Grassberger-Procaccia method [17, 36] and improves the uncertainty by more than one order of magnitude.

The robustness of this approach can be furtherly tested by affecting the Lorenz sequence with observational noise. The elements s_n of a noise-affected input sequence are given by

$$s_n = x_n + \eta_n,\tag{2.16}$$

where x_n are the elements of the Lorenz sequence, and η_n are independent identically distributed random variables, which are distributed according to a normal distribution with mean zero and variance σ_η^2 . The signal-to-noise-ratio (SNR) of a sequence is then defined as:

$$\text{SNR} = 20 \text{ dB } \log_{10} \left(\frac{\sigma_x}{\sigma_\eta} \right),\tag{2.17}$$

where $\sigma_x = 7.93$ is the standard deviation of the Lorenz sequence used in [24].

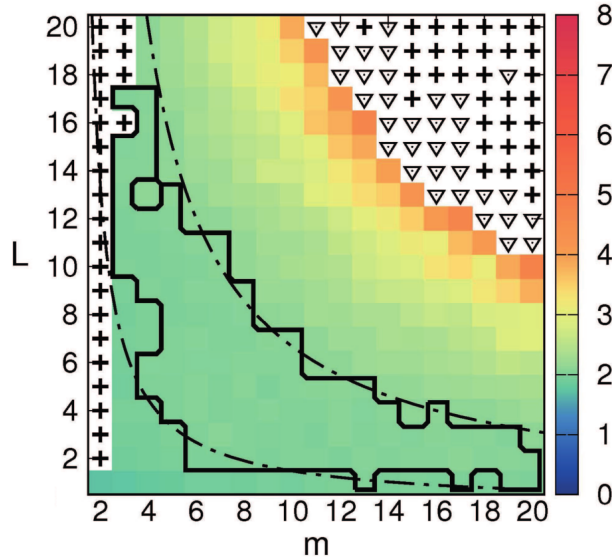


Figure 2.7: Correlation dimension of a Lorenz sequence as a function of the embedding parameters, using an embedding lattice $[2, 20] \times [1, 20]$. Embedding pairs marked with a “+” sign provide incompatibility with the requirement $\nu \leq m \leq \tau_I/(LT)$. Black triangles correspond to embedding pairs for which an evaluation of ν is unavailable due to the algorithm exceeding the computational time limit. The black solid line encompasses the lattice region corresponding to $\nu = 2.05 \pm 0.05$. The black dash-dotted curves are two hyperbolae bounding the region of uniform ν and are defined by $(m - 1)LT = 0.4$ and $(m - 1)LT = 1.8$. Figure adapted from Ref. [24].

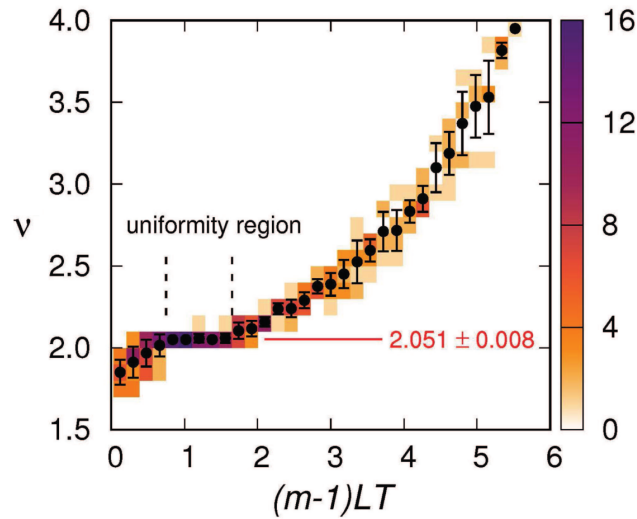


Figure 2.8: Sample joint distribution of the correlation dimension ν as a function of the embedding window $(m - 1)LT$ for the Lorenz sequence. Bin width is 0.1 along the ν axis and 0.18 along the $(m - 1)LT$ axis. Black dots and the related errorbars correspond to the expected value and the related uncertainty of ν for each given value (bin) of the embedding window. A uniformity region can be identified corresponding to embedding windows between 0.75 and 1.65. Averaging ν within the uniformity region yields 2.051 ± 0.008 . Figure adapted from Ref. [24].

The sample joint distributions of the Lorenz sequence contaminated by noise are shown in Fig. 2.9 for SNR equal to 30 dB (a), 20 dB (b) and 10 dB (c). The uniformity region can only be identified in the 30 dB case, although the corresponding estimated correlation dimension ν is about 15% higher with respect to the noiseless case.

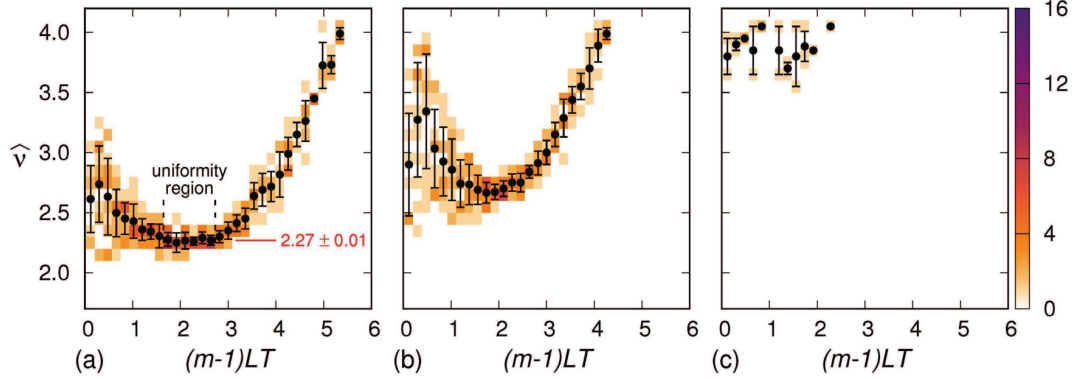


Figure 2.9: Sample joint distribution of the correlation dimension ν as a function of the embedding window $(m - 1)LT$ for the Lorenz sequence contaminated by noise. SNR are equal to 30 dB (a), 20 dB (b) and 10 dB (c). Bin width is 0.1 along the ν axis and 0.18 along the $(m - 1)LT$ axis. Black dots and the related errorbars correspond to the expected value and the related uncertainty of ν for each given value (bin) of the embedding window. A uniformity region can be identified only in the case in which $\text{SNR} = 30 \text{ dB}$. Figure adapted from Ref. [24].

In conclusion, the method described in Section 2.8 seems able to correctly identify chaotic sequences even in presence of noise, provided that the signal to noise ratio is not too large. In Chapter 3 this approach will be furtherly tested on the electronic implementation of the Burridge-Knopoff model.

Chapter 3

Chaos analysis of the electronic Burridge-Knopoff model

3.1 Two coupled blocks

Relying on the tools that have been introduced in Chapter 2, it is possible to analyze the chaotic behavior of a system starting from a time series. Considering the electronic implementation of the Burridge-Knopoff model that has been discussed in Chapter 1, we can thus analyze the double block behavior of the circuit (see Section 1.4).

The time series y_n was chosen to be the signal W_1 (see Fig. 1.3), which was sampled for 10 s with a sampling time of 0.1 ms, resulting in 10^5 points in the sequence. The driving voltage V_d was set to 0.05 V, since the chaotic behavior seems present only for $V_d \lesssim 0.11$ V (see Fig. 1.9). The results of the application of the “chasing chaos” method described in Section 2.8 are shown in Fig. 3.1.

In Fig. 3.1a the heatmap of the correlation dimension ν in the embedding lattice is shown. The two hyperbolae bound the uniformity region, which was chosen by searching for a plateau in the joint distribution in Fig. 3.1b. Carrying out a weighted average of the correlation dimension estimates in the uniformity region yields $\nu = 2.20 \pm 0.02$, which complies with the peak of the histogram in Fig. 3.1c, which is 2.20 ± 0.05 .

The estimates of the maximum Lyapunov exponent as a function of the embedding window are shown in Fig. 3.1d. Carrying out another weighted average of the MLE in the uniformity region yields $\text{MLE} = (54 \pm 1)$ Hz. Since the uniformity region is easy to be identified, it is reasonable to conclude that this system is chaotic. Nonetheless, the estimates of ν and MLE are assumed to be valid.

This chaos analysis was carried out also on a breadboard implementation of the circuit [4]. A uniformity region was identified and the correlation dimension was found to be $\nu = 1.971 \pm 0.007$. Regarding the MLE, a cluster of values at about 45 Hz occurred, which complied with the numerical value $\text{MLE} = (46 \pm 5)$ Hz, which was found integrating the differential equations of the system (Eq. 1.4) and applying the so-called standard method [37, 38].

Both the estimates for the correlation dimension and the maximum Lyapunov

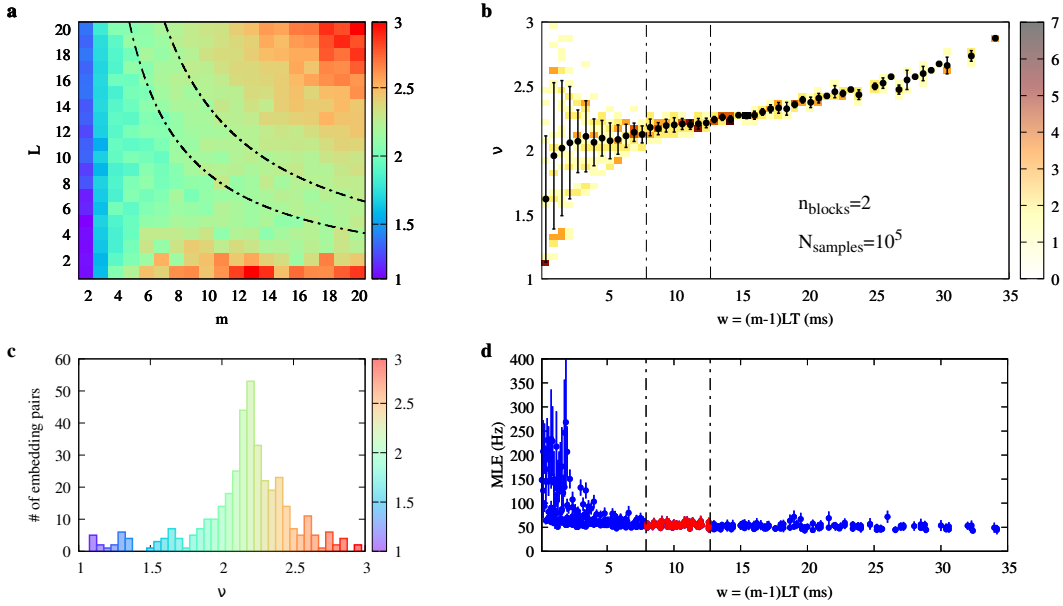


Figure 3.1: “Chasing chaos” analysis of the experimental W_1 time series obtained by setting $V_d = 0.05$ V with 2 coupled blocks. The number of elements in the sequence is 10^5 . (a) Map of estimated correlation dimension ν vs. embedding pair (m, L) . The black, dash-dotted hyperbolae bound the region of uniform ν corresponding to the interval of the embedding window w highlighted in (b) and (d). (b) Sample joint distribution of (w, ν) for the ν -map in (a). Black dots and the related errorbars correspond to the expected value and the related uncertainty of ν for each given value (bin) of w . A uniformity region, highlighted by the dash-dotted vertical lines, is identified. (c) Histogram of the estimated ν . (d) Distribution of MLE as a function of w . Each point and the related uncertainty corresponds to the value assessed on an embedding pair by using the divergence rate method. A cluster of points, marked in red, can be identified in the uniformity region of (b), also highlighted here.

exponent are larger in the integrated board case with respect to the breaboard case. A possible explanation for this is the higher presence of noise in the integrated board; as was discussed in Section 2.8.1, the correlation dimension evaluation increases with noise.

Nevertheless, the chaotic dynamics is observed in both implementations. The calculations of ν and MLE strongly depend on many factors, such as the embedding lattice, the sampling time, or the arbitrariness on the choice of the uniformity region. Thus, the results on the two implementations are assumed to be in compliance with each other.

3.2 Three coupled blocks

After establishing that the system constituted of two coupled blocks is chaotic, it can be interesting to observe what happens when more than two blocks are coupled, starting for now from three. In particular, assuming that the chaotic behavior is

preserved, the interesting part is the dependence of ν and MLE on the number of coupled blocks.

Something to be considered when dealing with three or more coupled blocks is the choice of the time series. In the two blocks case, choosing W_1 or W_2 was perfectly equivalent. In the three blocks case, instead, we can distinguish between blocks on the “boundary” (block 1 and block 3) and blocks in the “center” (block 2). Takens’ theorem [19] states that the results of the embedding procedure should be independent of the choice of the state variable; once again, this is true for noiseless, finely sampled and infinitely long sequences. It is thus reasonable to perform the analysis in both cases.

3.2.1 Block on the boundary

The time series y_n was chosen to be the signal W_1 (block on the boundary), which was sampled for 10 s with a sampling time of 0.1 ms, resulting in 10^5 points in the sequence. The driving voltage V_d was kept at 0.05 V. The results of the application of the “chasing chaos” method are shown in Fig. 3.2.

Using the same methods employed in the previous section, the correlation dimension averaged on the uniformity region yields $\nu = 2.21 \pm 0.04$, which complies with the histogram peak which is at 2.25 ± 0.05 . The maximum Lyapunov exponent in the uniformity region was found to be equal to $\text{MLE} = (453 \pm 6)$ Hz.

The system is once again chaotic, and both ν and MLE have increased with respect to the values found in the two blocks case. In particular, while the increment of the correlation dimension is small, the MLE changes by an order of magnitude. This might hint to the fact that ν depends linearly on the number of coupled blocks, while the MLE has an exponential dependence; this will be unraveled in Section 3.4.

Something that should be taken into account is that the choice on the sampling time might be improved. The reason for this is that the uniformity region is found at very small values of the embedding window (see Fig. 3.2) with respect to the total time spanned by the embedding lattice. This means that reducing the sampling time might increase the number of points in the uniformity region, thus improving the estimates on ν and MLE.

Another “chasing chaos” analysis was then carried out by setting the sampling time to 0.05 ms, doubling the number of elements in the time series, i.e. 2×10^5 . The results are shown in Fig. 3.3.

The new estimate for the correlation dimension yields $\nu = 2.27 \pm 0.02$, which complies with the histogram peak which is at 2.260 ± 0.035 . The maximum Lyapunov exponent in the uniformity region was found to be equal to $\text{MLE} = (439 \pm 4)$ Hz.

These estimates are very similar to the results obtained with 10^5 points. Nonetheless, the errors have slightly been improved, and the plateau is more visible and contains more points. This change in the sampling time will be much more relevant when dealing with systems with many coupled blocks.

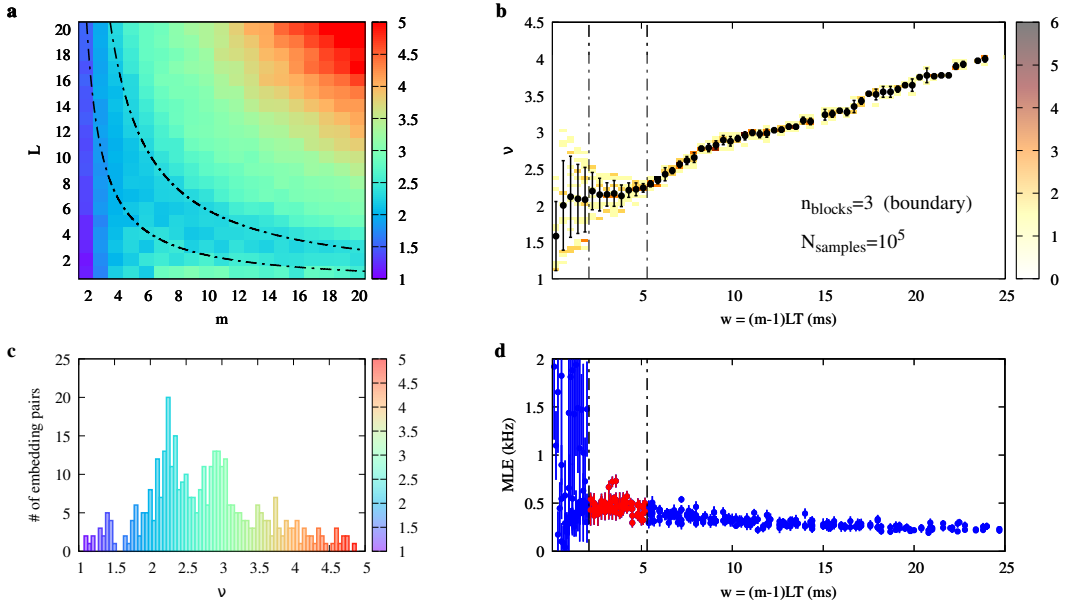


Figure 3.2: “Chasing chaos” analysis of the experimental W_1 time series obtained by setting $V_d = 0.05$ V with 3 coupled blocks. The number of elements in the sequence is 10^5 . (a) Map of estimated correlation dimension ν vs. embedding pair (m, L) . The black, dash-dotted hyperbolae bound the region of uniform ν corresponding to the interval of the embedding window w highlighted in (b) and (d). (b) Sample joint distribution of (w, ν) for the ν -map in (a). Black dots and the related errorbars correspond to the expected value and the related uncertainty of ν for each given value (bin) of w . A uniformity region, highlighted by the dash-dotted vertical lines, is identified. (c) Histogram of the estimated ν . (d) Distribution of MLE as a function of w . Each point and the related uncertainty corresponds to the value assessed on an embedding pair by using the divergence rate method. A cluster of points, marked in red, can be identified in the uniformity region of (b), also highlighted here.

3.2.2 Block in the center

The chaos analysis was then carried out on the time series obtained by sampling the signal W_2 (block in the center) with a sampling time of 0.05 ms, resulting in 2×10^5 elements of the sequence. The results are shown in Fig. 3.4.

The estimates for the correlation dimension and the maximum Lyapunov exponent yield $\nu = 2.34 \pm 0.04$ and $\text{MLE} = (427 \pm 4)$ Hz. While the MLE is practically the same as the boundary case, the correlation dimension is slightly larger; the uncertainty on ν is also increased. In order to make a guess on the reasons why this discrepancy occurs it is necessary to consider the oscilloscope quantization, as will be done in the following section.

The difference between the two cases can also be appreciated by looking at the attractor plots, shown in Fig. 3.5. The signals taken from the center block seems to be “more chaotic”, in the sense that the phase space is explored more in the same amount of time. Intuitively, since the block in the center is linked to two blocks

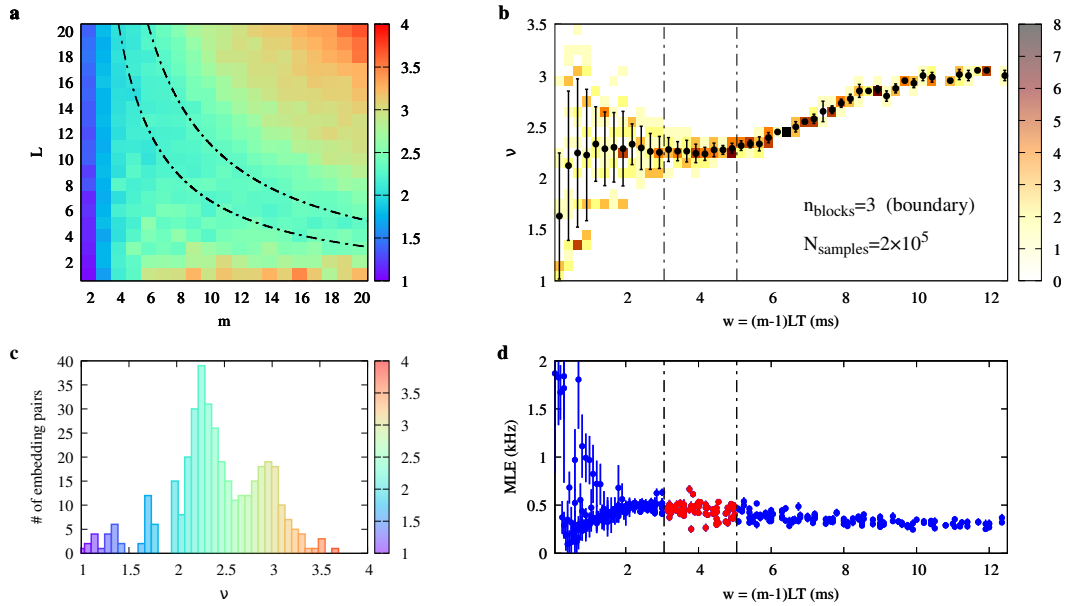


Figure 3.3: “Chasing chaos” analysis of the experimental W_1 time series obtained by setting $V_d = 0.05$ V with 3 coupled blocks. The number of elements in the sequence is 2×10^5 . (a) Map of estimated correlation dimension ν vs. embedding pair (m, L) . The black, dash-dotted hyperbolae bound the region of uniform ν corresponding to the interval of the embedding window w highlighted in (b) and (d). (b) Sample joint distribution of (w, ν) for the ν -map in (a). Black dots and the related errorbars correspond to the expected value and the related uncertainty of ν for each given value (bin) of w . A uniformity region, highlighted by the dash-dotted vertical lines, is identified. (c) Histogram of the estimated ν . (d) Distribution of MLE as a function of w . Each point and the related uncertainty corresponds to the value assessed on an embedding pair by using the divergence rate method. A cluster of points, marked in red, can be identified in the uniformity region of (b), also highlighted here.

instead of one, it seems reasonable that the signal is, once again, “more chaotic”. However, this should not modify the estimates of ν and MLE, since W_2 and W_1 are both variables of the same system of differential equations. This means that there is some “experimental” reason for which this strange behavior is observed.

3.3 The effects of the oscilloscope quantization

One of the possible reasons for which the results of the chaos analysis differ between W_1 and W_2 might lay in the quantization of the oscilloscope, with which the signals are sampled. The data read by the oscilloscope are stored in a finite number of bits, namely eight. When dealing with chaotic signals, i.e. with sharp peaks and rapid changes of the signal, this quantization reduces the information given by a time series; moreover, it can introduce spurious contributions that can modify the estimates on the correlation dimension and the maximum Lyapunov exponent.

In order to test the actual effects of this quantization on the analysis, the following

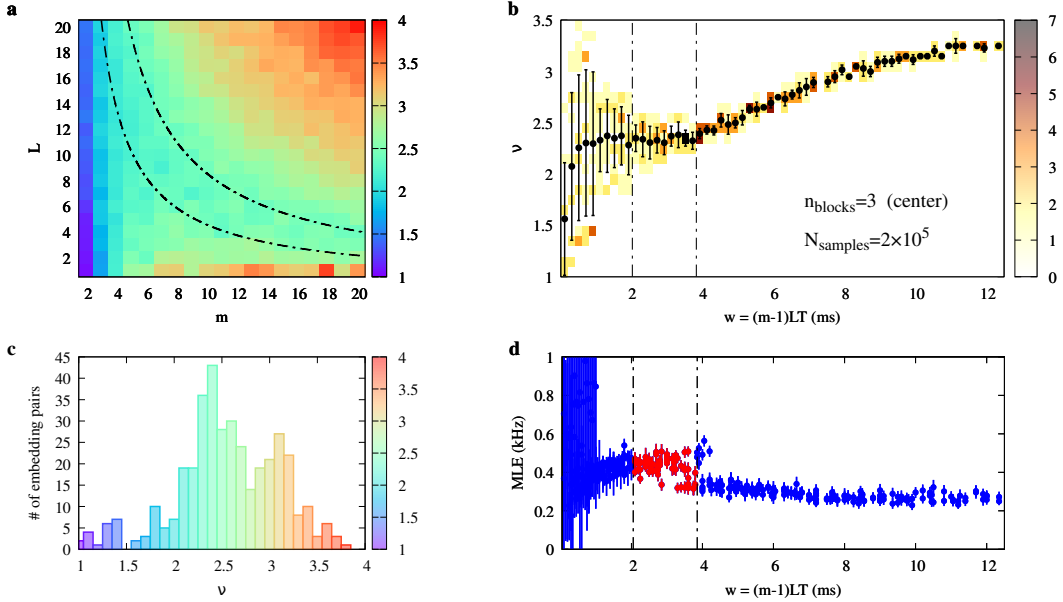


Figure 3.4: “Chasing chaos” analysis of the experimental W_2 time series obtained by setting $V_d = 0.05$ V with 3 coupled blocks. The number of elements in the sequence is 2×10^5 . (a) Map of estimated correlation dimension ν vs. embedding pair (m, L) . The black, dash-dotted hyperbolae bound the region of uniform ν corresponding to the interval of the embedding window w highlighted in (b) and (d). (b) Sample joint distribution of (w, ν) for the ν -map in (a). Black dots and the related errorbars correspond to the expected value and the related uncertainty of ν for each given value (bin) of w . A uniformity region, highlighted by the dash-dotted vertical lines, is identified. (c) Histogram of the estimated ν . (d) Distribution of MLE as a function of w . Each point and the related uncertainty corresponds to the value assessed on an embedding pair by using the divergence rate method. A cluster of points, marked in red, can be identified in the uniformity region of (b), also highlighted here.

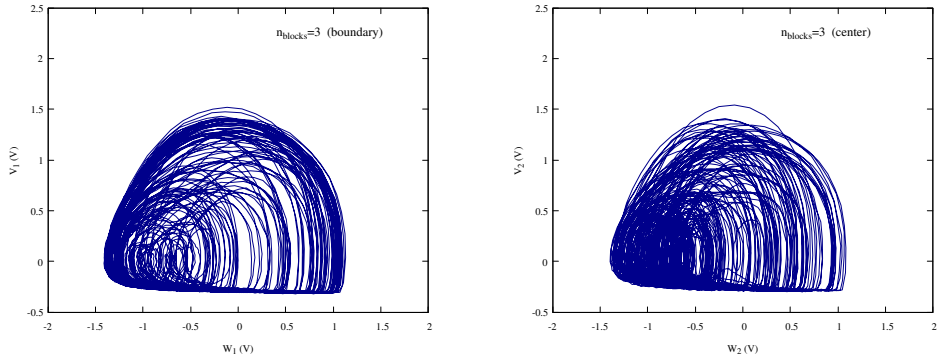


Figure 3.5: Phase portraits of V vs W for 3 coupled blocks, analyzing the block on the boundary (left) and in the center (right), for a total time of 5 s, setting $V_d = 0.05$ V.

method was employed.

- Given the signal y_n , the smallest separation between two successive elements

y_n, y_{n+1} , i.e. the oscilloscope quantization, is searched for. For example, if the signal is:

$$\{y_n\} = (1.5, 1.5, 1.75, 2, 2.5, 2.75),$$

the quantization is 0.25.

- The signal is then divided by the quantization, so that each element becomes an integer ($y_n \rightarrow y_n^{\text{int}}$). In the example, the signal y_n becomes:

$$\{y_n^{\text{int}}\} = \left\{ \frac{y_n}{0.25} \right\} = (6, 6, 7, 8, 10, 11).$$

- Then an integer division is performed on the signal, i.e. y_n^{int} is first divided by two, then rounded to the lowest integer and multiplied by two again ($y_n^{\text{int}} \rightarrow \tilde{y}_n^{\text{int}}$). Our example sequence then becomes:

$$\{\tilde{y}_n^{\text{int}}\} = (6, 6, 6, 8, 10, 10).$$

- In the end, the resulting sequence is multiplied by the quantization, so that:

$$\{\tilde{y}_n\} = (1.5, 1.5, 1.5, 2, 2.5, 2.5).$$

The time series $\{\tilde{y}_n\}$ obtained at the end of this process is very similar to the starting sequence y_n , with the difference that the quantization is doubled. Therefore, carrying out the chasing chaos analysis on both sequences should give an idea on the effect of the quantization on the estimates of ν and MLE.

The analysis was then carried out on the system of four coupled blocks. The starting signal was chosen to be W_1 , from which the double quantized signal \tilde{W}_1 was obtained. In order to improve the reasoning, also the quadrupled quantized signal $\tilde{\tilde{W}}_1$ was analyzed. The graphical results of these analyses are shown in Appendix A. The estimates of ν and MLE in the three cases are presented in Table 3.1.

| | ν | MLE (kHz) |
|-----------------------|-----------------|-----------------|
| W_1 | 2.29 ± 0.03 | 1.03 ± 0.04 |
| \tilde{W}_1 | 2.36 ± 0.06 | 1.05 ± 0.05 |
| $\tilde{\tilde{W}}_1$ | 2.54 ± 0.11 | 0.87 ± 0.06 |

Table 3.1: Estimates of ν and MLE on the system of four coupled blocks. W_1 is the signal given by the oscilloscope, while \tilde{W}_1 and $\tilde{\tilde{W}}_1$ are obtained from W_1 by doubling and quadrupling the quantization, respectively.

The MLE is not too sensible to the oscilloscope quantization, since it has an observable decrease only in the quadrupled quantization case. On the other hand, both the correlation dimension and its uncertainty significantly increase with the quantization. This results are consistent with the discrepancies found in the three blocks case between the boundary block and the center block, hinting to the fact that the oscilloscope quantization might play a compelling role in the chaos analysis.

3.4 Multiple coupled blocks

It is now possible to fully utilize the integrated board, coupling an arbitrary number of blocks and studying the chaotic dynamics that comes with it. In particular, the chaos analysis was carried out with the number of coupled blocks ranging from 2 to 25, always choosing W_1 as the time series, i.e. a block on the boundary. When the number of coupled blocks was odd, an additional analysis was carried out on the signal W_k , where the k -th block is located in the center (e.g. in the 7 blocks case, the analyzed signal will be W_4). The driving voltage was always set equal to 0.05 V, and the number of elements in the sequence was always kept at 2×10^5 . The graphical results of these analyses are shown in Appendix B.

The correlation dimension and the maximum Lyapunov exponent as a function of the number of coupled blocks are shown in Fig. 3.6 for both the boundary blocks and the center blocks.

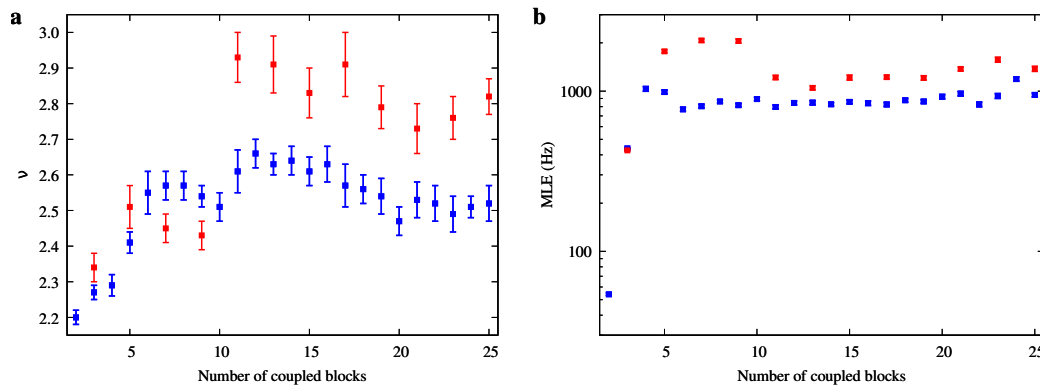


Figure 3.6: Correlation dimension (a) and maximum Lyapunov exponent (b) estimates as a function of the number of coupled blocks. The blue points represent blocks on the boundary, while the red ones represent blocks in the center.

The correlation dimension of the boundary blocks increases noticeably fast up until 6 coupled blocks, from which ν seems to fluctuate around a plateau value $\nu_{\text{pl}} = 2.56 \pm 0.01$, which was obtained from a weighted average of the ν values from 6 to 25 coupled blocks.

Regarding the center blocks instead, the majority of the ν values are larger with respect to the corresponding estimates on the boundary blocks, and the same goes for the uncertainties. A possible reason for this behavior can be once again the oscilloscope quantization. As can be seen from the attractor plots in Fig. 3.7, the explored region of the phase space is smaller when looking at center blocks. This means that the oscilloscope quantization is more relevant in this case, resulting in higher estimates of the correlation dimension.

Regarding the maximum Lyapunov exponent for the boundary blocks, its rapid increase stops at 4 coupled blocks, from which it starts fluctuating around a plateau of about 865 Hz. Once again, the MLE values estimated using the center blocks are larger than the boundary ones. This cannot be explained with the oscilloscope

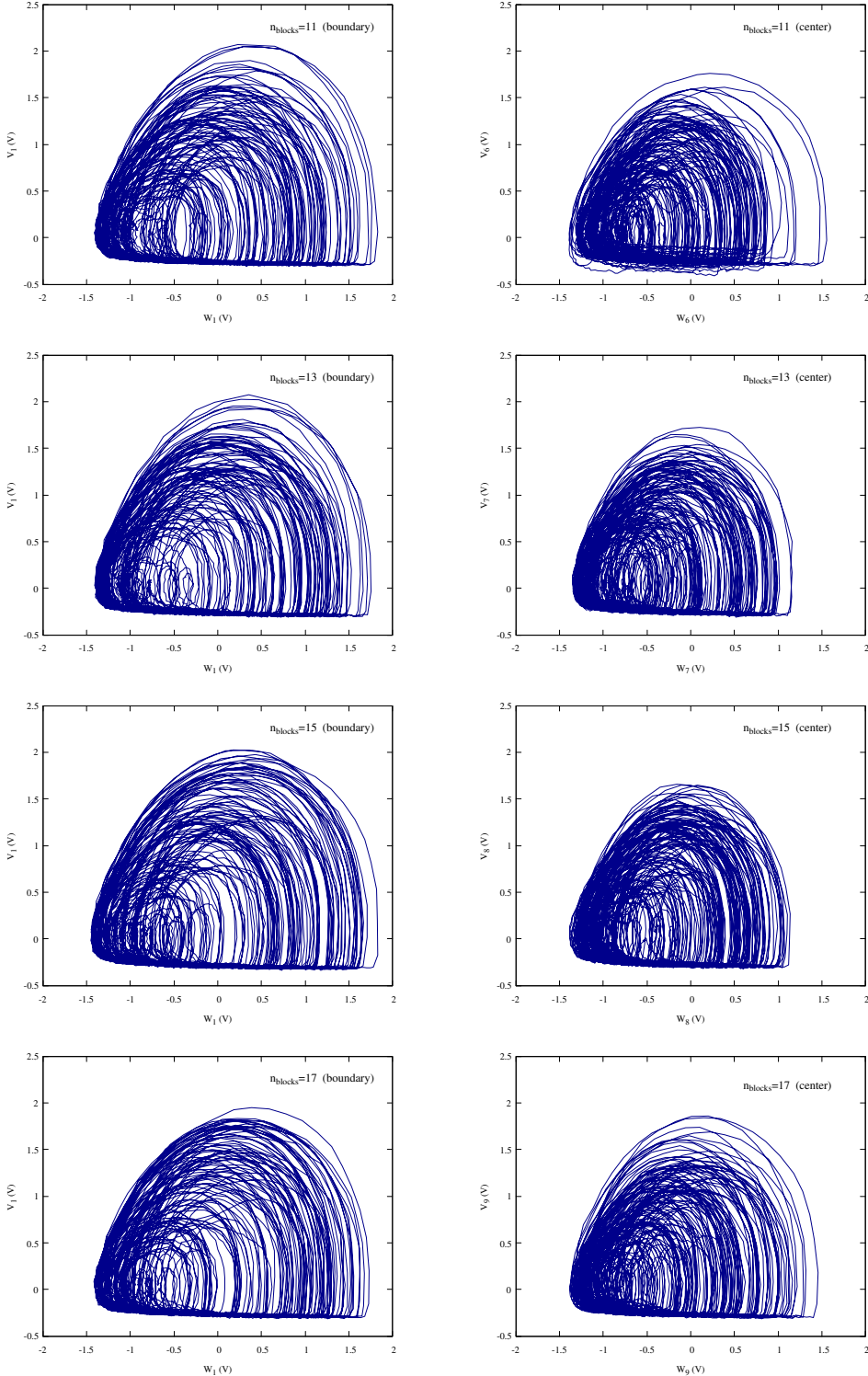


Figure 3.7: Phase portraits of V vs W from 11 to 17 coupled blocks, analyzing the block on the boundary (left) and in the center (right), for a total time of 5 s, setting $V_d = 0.05$ V.

quantization, since the dependence of the MLE on it is very weak; moreover, the MLE should decrease with the quantization, while here it increases.

An important consideration in this regard is the following. In Fig. 3.8 and Fig. 3.9

the results of the chaos analysis for 13 coupled blocks are shown, for the boundary and center case respectively.

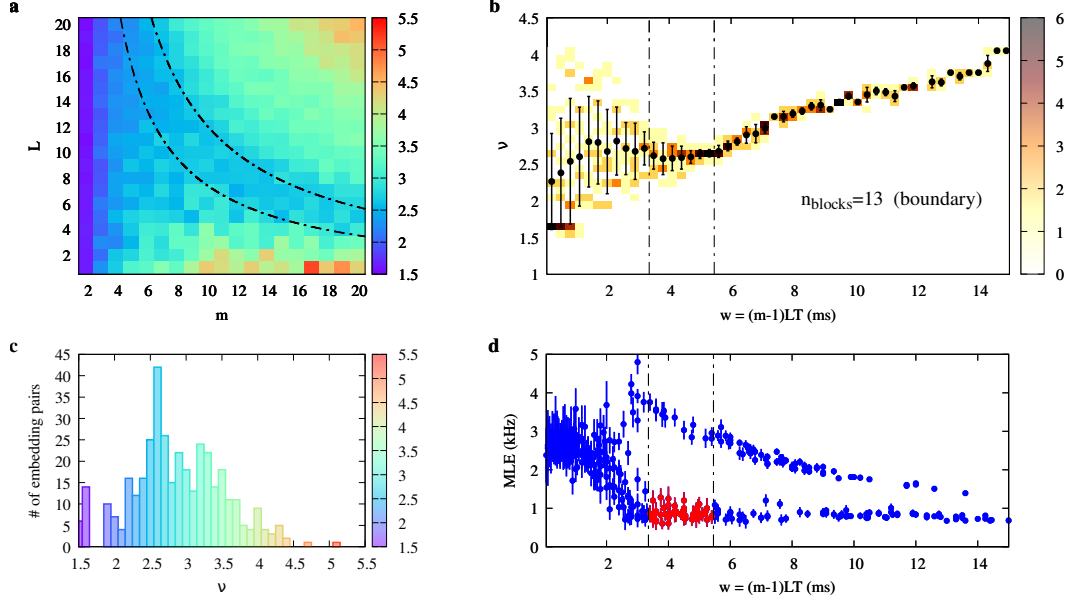


Figure 3.8: “Chasing chaos” analysis of the experimental W_1 time series with 13 coupled blocks. (a) Map of estimated correlation dimension ν vs. embedding pair (m, L) . (b) Sample joint distribution of (w, ν) for the ν -map in (a). (c) Histogram of the estimated ν . (d) Distribution of MLE as a function of w .

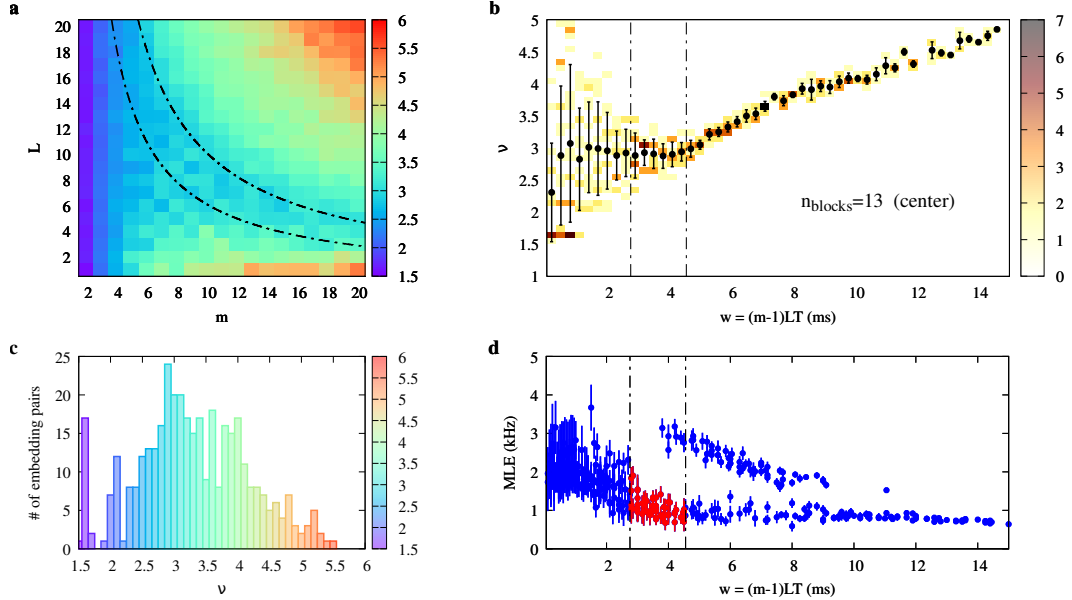


Figure 3.9: “Chasing chaos” analysis of the experimental W_7 time series with 13 coupled blocks. (a) Map of estimated correlation dimension ν vs. embedding pair (m, L) . (b) Sample joint distribution of (w, ν) for the ν -map in (a). (c) Histogram of the estimated ν . (d) Distribution of MLE as a function of w .

In both cases, the various MLE points in the uniformity region are subdivided in two different clusters¹. This hints at the possibility that there is more than one positive Lyapunov exponent in the system. Since the divergence rate method is optimal when dealing with only one positive exponent, it is likely that a systematic error of the method occurs.

In any case, the two plateaux for the boundary and center case are, respectively, $\text{MLE}_{\text{boundary}} = 865 \text{ Hz}$ and $\text{MLE}_{\text{center}} = 1361 \text{ Hz}$. The MLE can then be estimated, in a simplistic manner, as the average between these values, i.e. $\text{MLE} = (1.11 \pm 0.25) \text{ kHz}$, where the error is simply given by half of the difference between $\text{MLE}_{\text{boundary}}$ and $\text{MLE}_{\text{center}}$. The systematic error on this estimate is not negligible and is indeed a big limit of the divergence rate method. However, this value of MLE is meaningful, since the characteristic time of the circuit (see Fig. 1.3) is given by $\tau = RC = 1 \text{ ms}$; therefore, the characteristic frequency of the circuit is 1 kHz, which complies with our estimate of the MLE.

¹For the analysis, only the most populated clusters, i.e. the ones highlighted in red in the plots, were considered.

Appendices

Appendix A

Chaos analysis for oscilloscope quantization

The following plots represent the chaotic behavior of the system of four coupled blocks, in which the oscilloscope quantization is progressively increased (see Section 3.3). For these analyses the driving voltage V_d is always set to 0.05 V, and the number of points in the sampled sequences is always 2×10^5 .

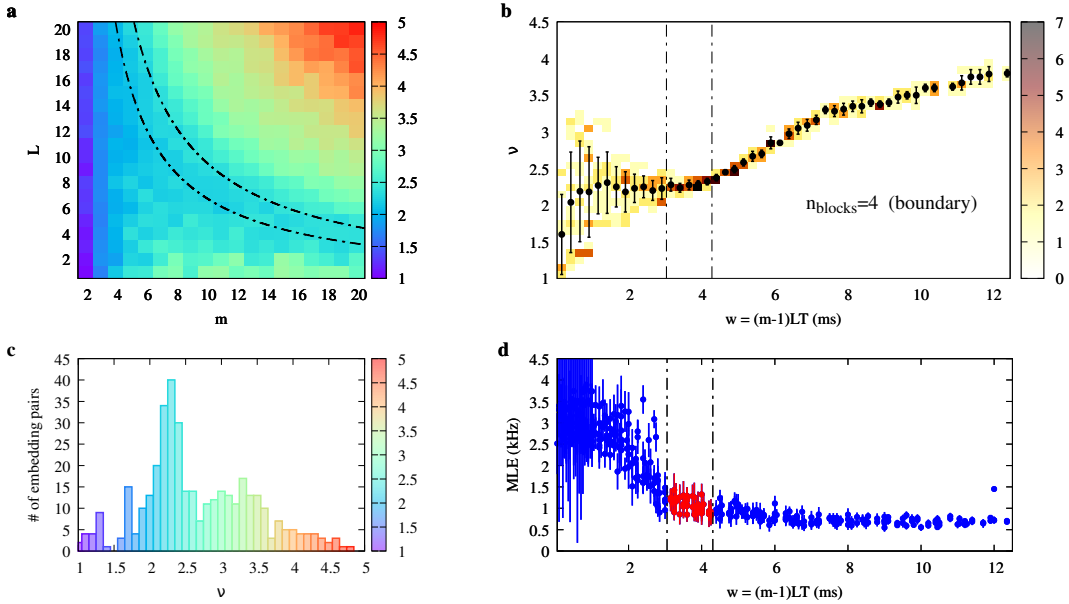


Figure A.1: “Chasing chaos” analysis of the experimental W_1 time series with 4 coupled blocks. (a) Map of estimated correlation dimension ν vs. embedding pair (m, L) . (b) Sample joint distribution of (w, ν) for the ν -map in (a). (c) Histogram of the estimated ν . (d) Distribution of MLE as a function of w .

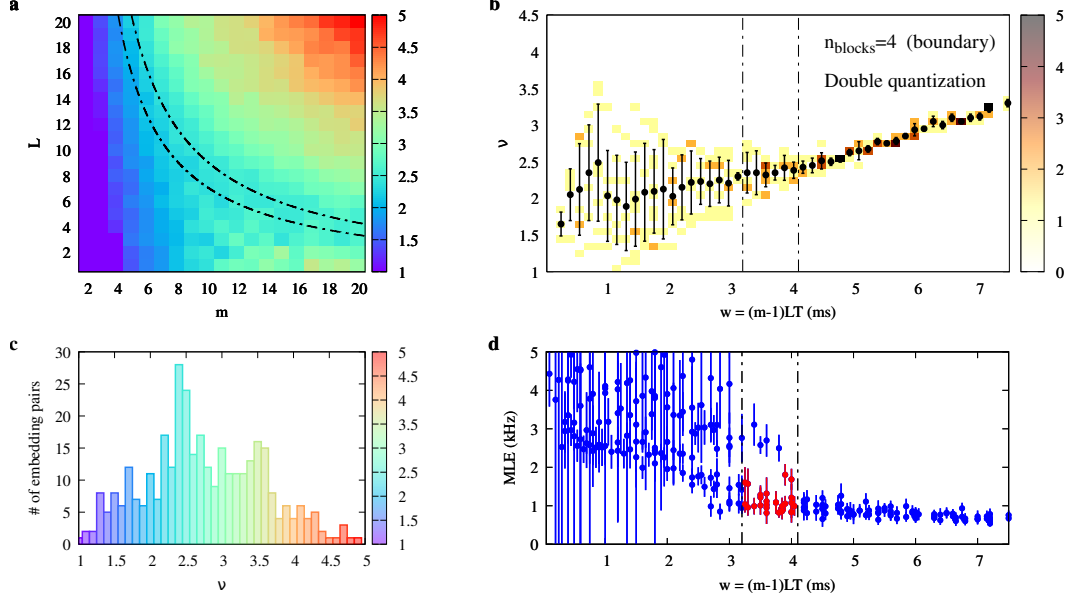


Figure A.2: “Chasing chaos” analysis of the experimental \tilde{W}_1 time series with 4 coupled blocks. The oscilloscope quantization is doubled with respect to the case in Fig. A.1 (a) Map of estimated correlation dimension ν vs. embedding pair (m, L) . (b) Sample joint distribution of (w, ν) for the ν -map in (a). (c) Histogram of the estimated ν . (d) Distribution of MLE as a function of w .

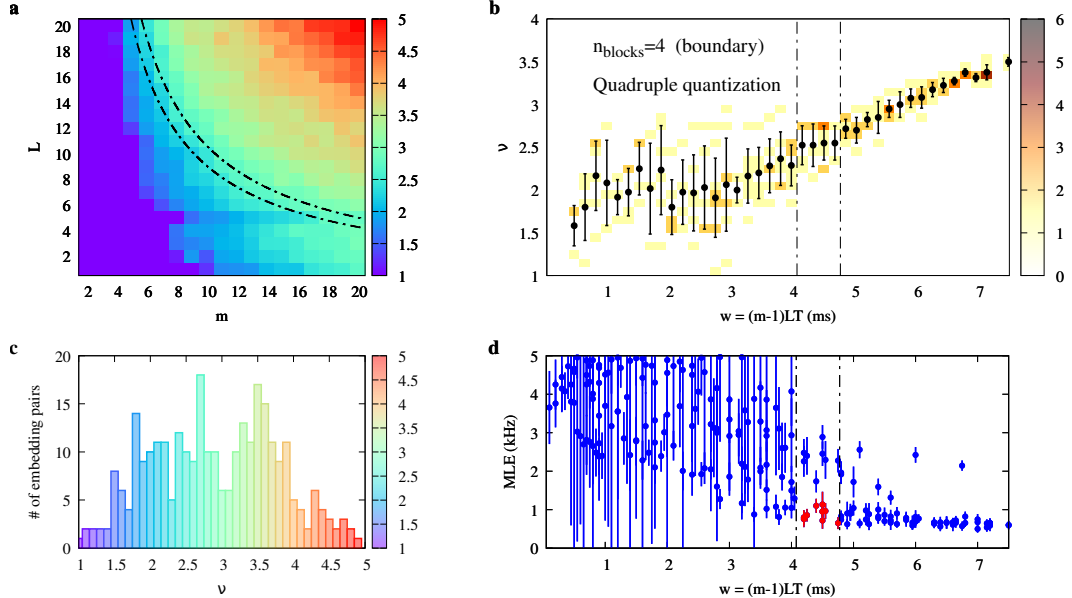


Figure A.3: “Chasing chaos” analysis of the experimental \tilde{W}_1 time series with 4 coupled blocks. The oscilloscope quantization is quadrupled with respect to the case in Fig. A.1 (a) Map of estimated correlation dimension ν vs. embedding pair (m, L) . (b) Sample joint distribution of (w, ν) for the ν -map in (a). (c) Histogram of the estimated ν . (d) Distribution of MLE as a function of w .

Appendix B

Chaos analysis on multiple coupled blocks

The following plots represent the chaotic behavior of the system from 5 to 25 coupled blocks (excluding 13 since it is presented in Section 3.4), using the signal W_1 as the time series. When the number of blocks is odd, an additional analysis was carried out on the signal W_k , where the k -th block is located in the center (e.g. in the seven blocks case, the analyzed signal will be W_4). For these analyses the driving voltage V_d is always set to 0.05 V, and the number of points in the sampled sequences is always 2×10^5 .

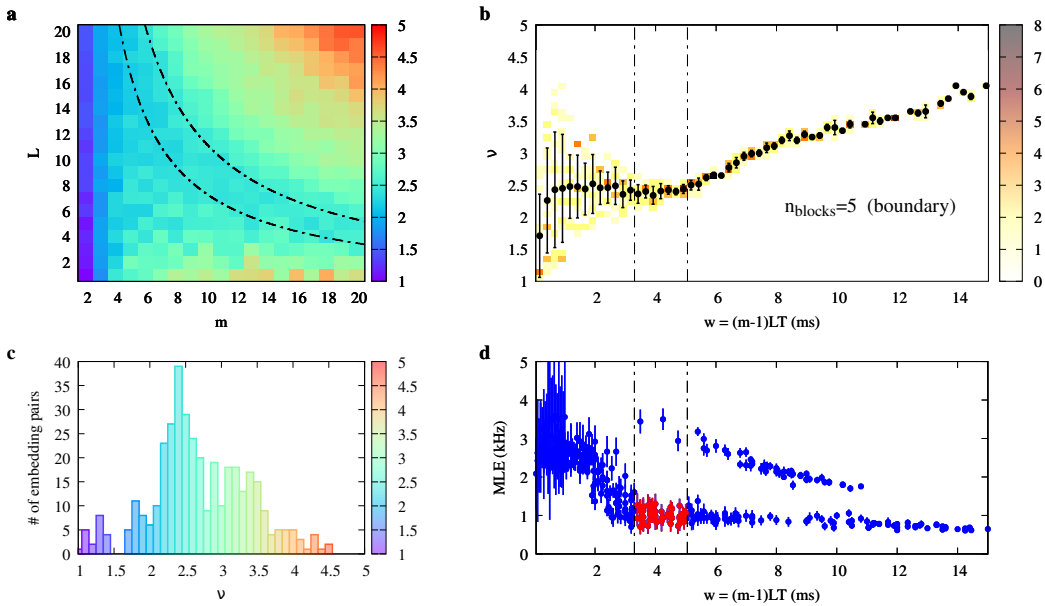


Figure B.1: “Chasing chaos” analysis of the experimental W_1 time series with 5 coupled blocks. (a) Map of estimated correlation dimension ν vs. embedding pair (m, L) . (b) Sample joint distribution of (w, ν) for the ν -map in (a). (c) Histogram of the estimated ν . (d) Distribution of MLE as a function of w .

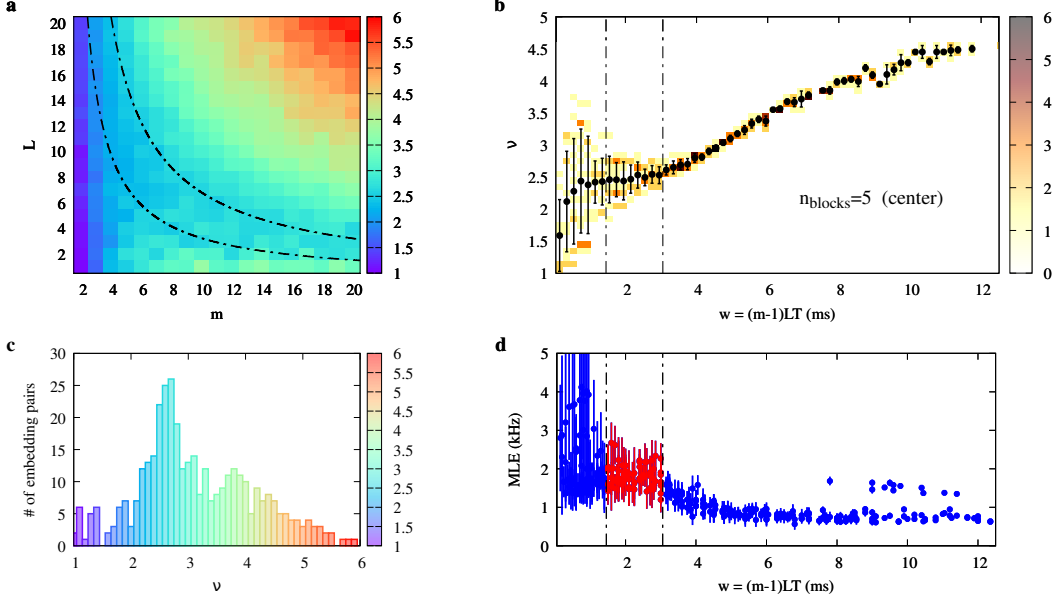


Figure B.2: “Chasing chaos” analysis of the experimental W_3 time series with 5 coupled blocks. (a) Map of estimated correlation dimension ν vs. embedding pair (m, L) . (b) Sample joint distribution of (w, ν) for the ν -map in (a). (c) Histogram of the estimated ν . (d) Distribution of MLE as a function of w .

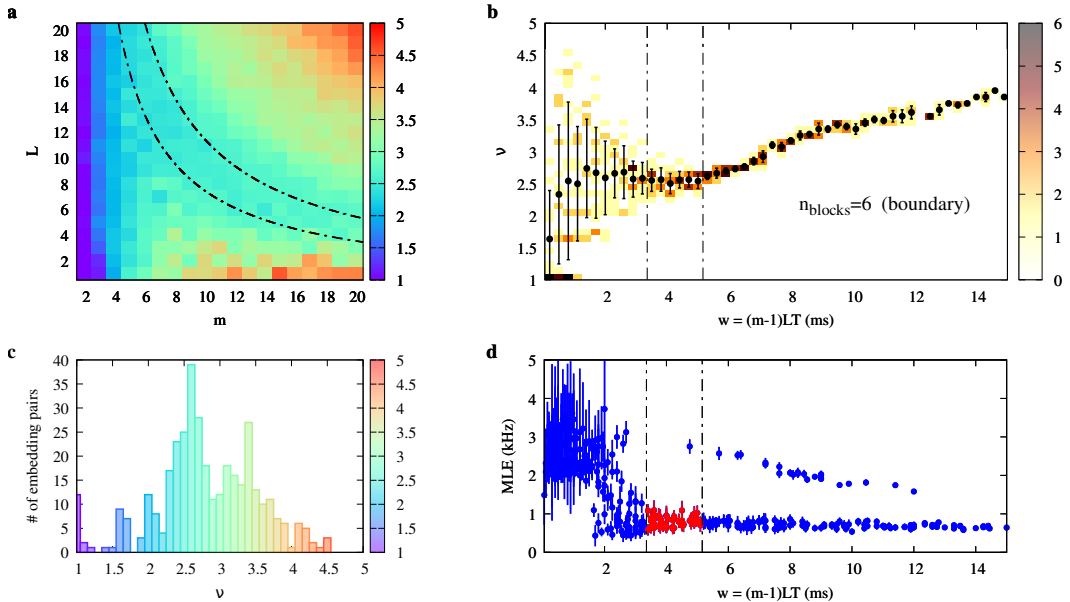


Figure B.3: “Chasing chaos” analysis of the experimental W_1 time series with 6 coupled blocks. (a) Map of estimated correlation dimension ν vs. embedding pair (m, L) . (b) Sample joint distribution of (w, ν) for the ν -map in (a). (c) Histogram of the estimated ν . (d) Distribution of MLE as a function of w .

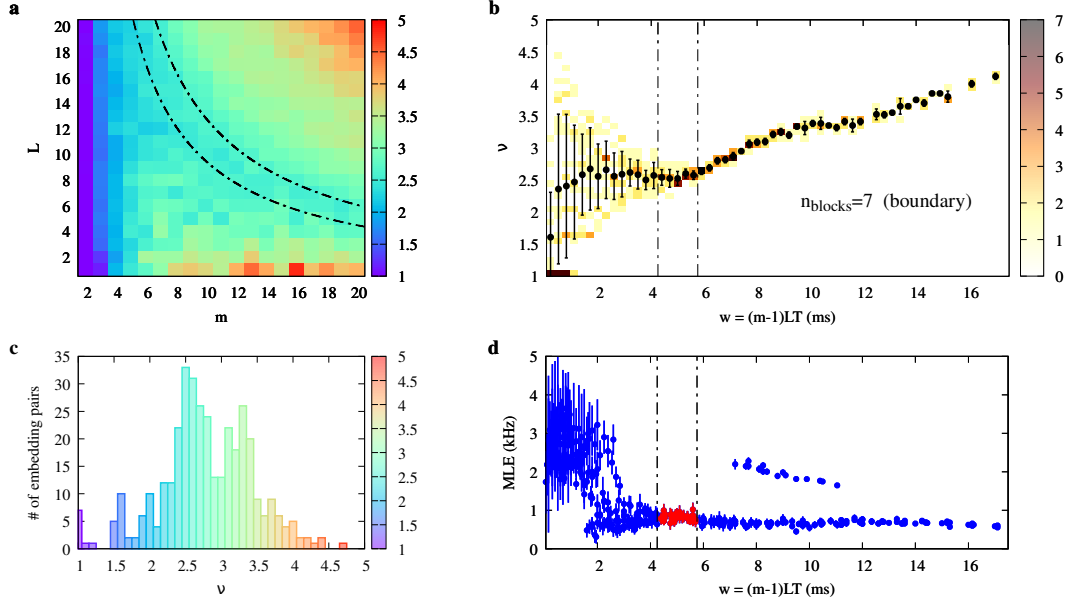


Figure B.4: “Chasing chaos” analysis of the experimental W_1 time series with 7 coupled blocks. (a) Map of estimated correlation dimension ν vs. embedding pair (m, L) . (b) Sample joint distribution of (w, ν) for the ν -map in (a). (c) Histogram of the estimated ν . (d) Distribution of MLE as a function of w .

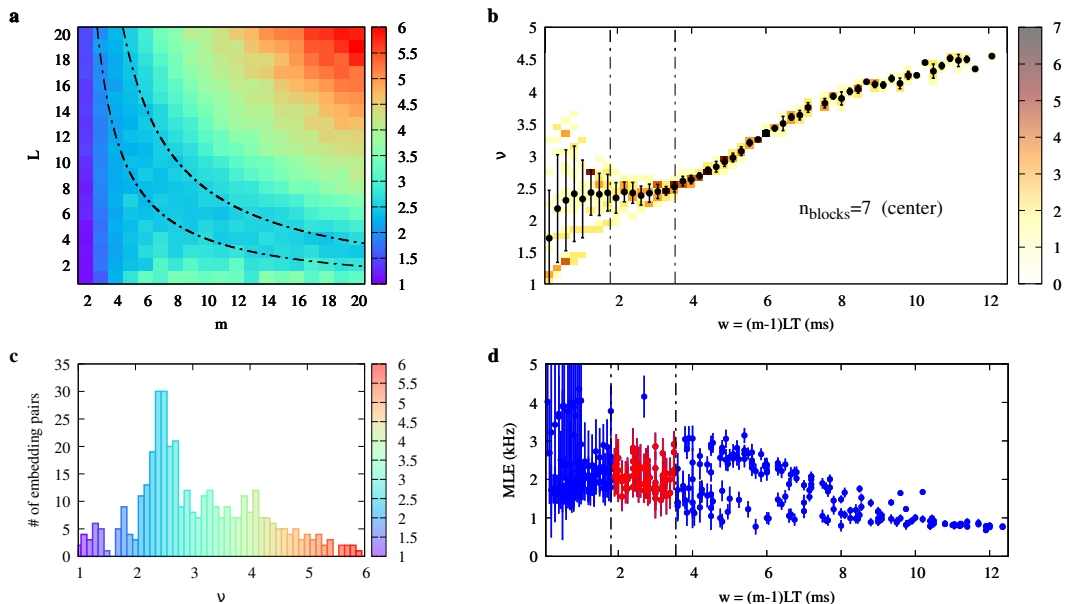


Figure B.5: “Chasing chaos” analysis of the experimental W_4 time series with 7 coupled blocks. (a) Map of estimated correlation dimension ν vs. embedding pair (m, L) . (b) Sample joint distribution of (w, ν) for the ν -map in (a). (c) Histogram of the estimated ν . (d) Distribution of MLE as a function of w .

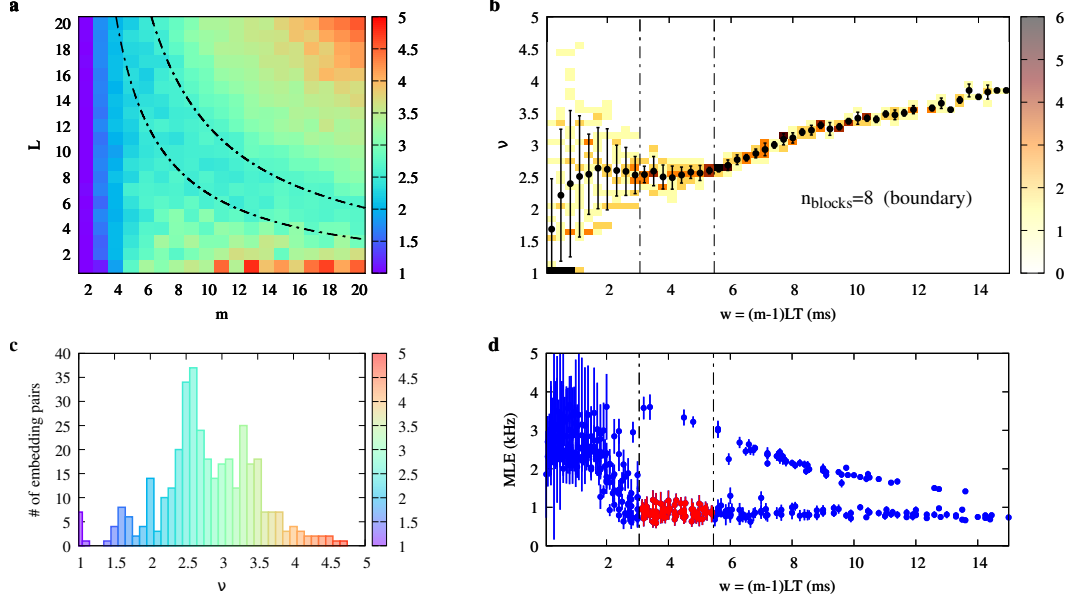


Figure B.6: “Chasing chaos” analysis of the experimental W_1 time series with 8 coupled blocks. (a) Map of estimated correlation dimension ν vs. embedding pair (m, L) . (b) Sample joint distribution of (w, ν) for the ν -map in (a). (c) Histogram of the estimated ν . (d) Distribution of MLE as a function of w .

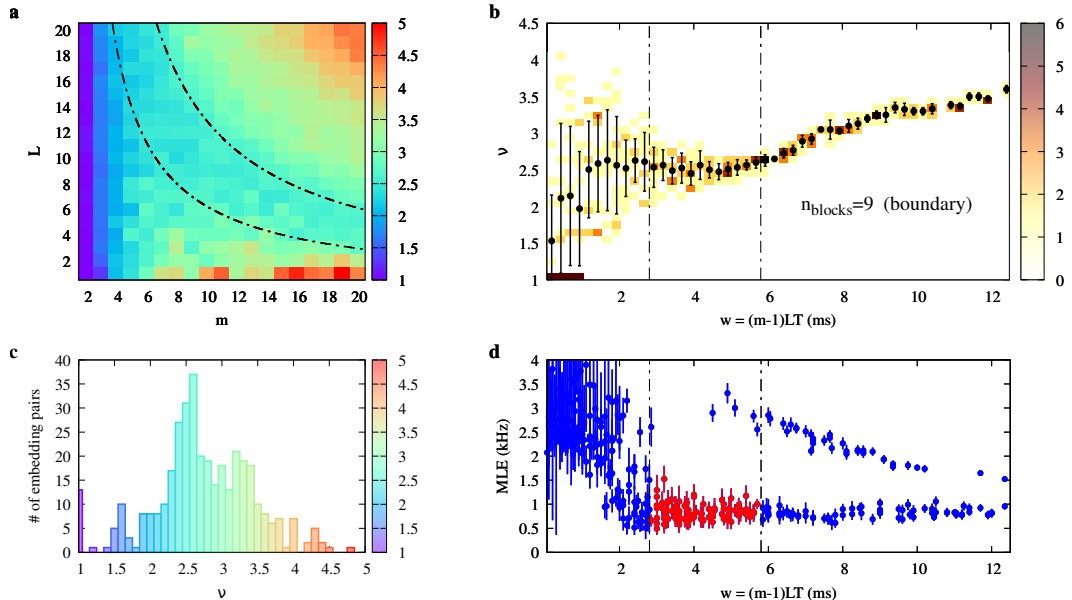


Figure B.7: “Chasing chaos” analysis of the experimental W_1 time series with 9 coupled blocks. (a) Map of estimated correlation dimension ν vs. embedding pair (m, L) . (b) Sample joint distribution of (w, ν) for the ν -map in (a). (c) Histogram of the estimated ν . (d) Distribution of MLE as a function of w .

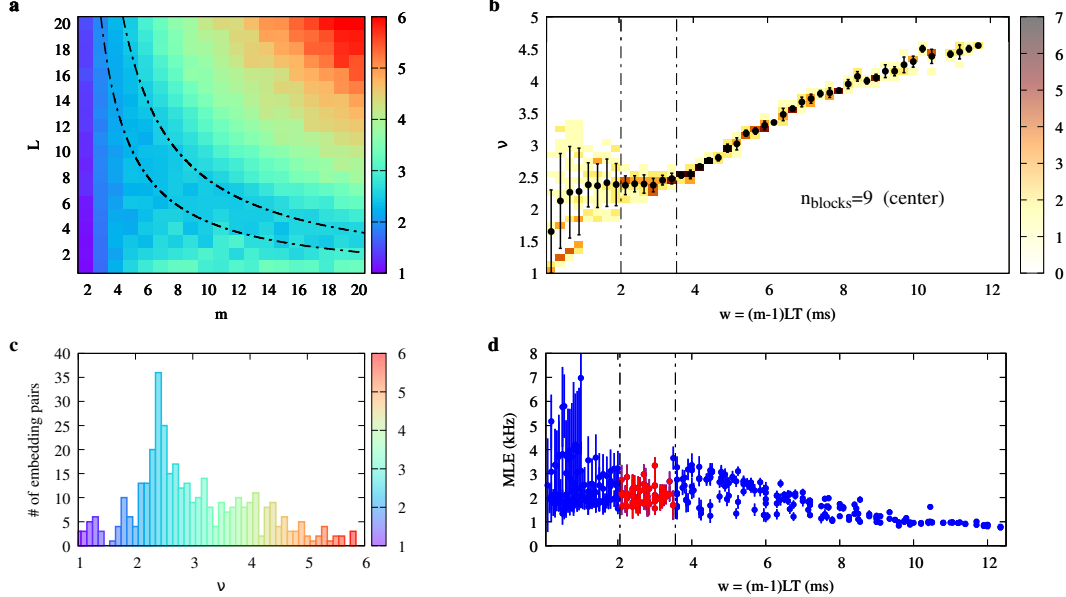


Figure B.8: “Chasing chaos” analysis of the experimental W_5 time series with 9 coupled blocks. (a) Map of estimated correlation dimension ν vs. embedding pair (m, L) . (b) Sample joint distribution of (w, ν) for the ν -map in (a). (c) Histogram of the estimated ν . (d) Distribution of MLE as a function of w .

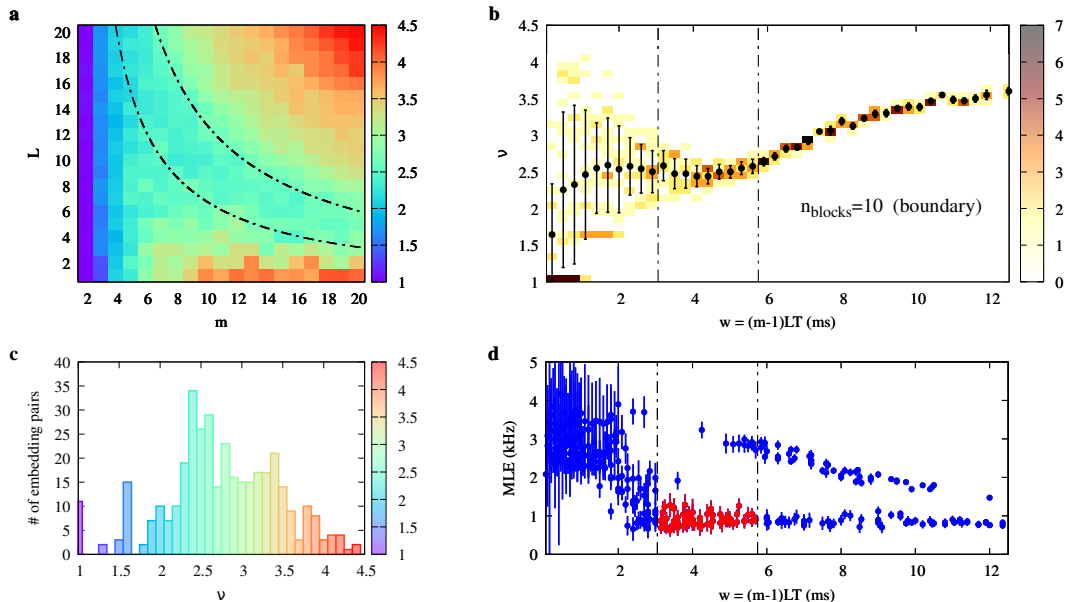


Figure B.9: “Chasing chaos” analysis of the experimental W_1 time series with 10 coupled blocks. (a) Map of estimated correlation dimension ν vs. embedding pair (m, L) . (b) Sample joint distribution of (w, ν) for the ν -map in (a). (c) Histogram of the estimated ν . (d) Distribution of MLE as a function of w .

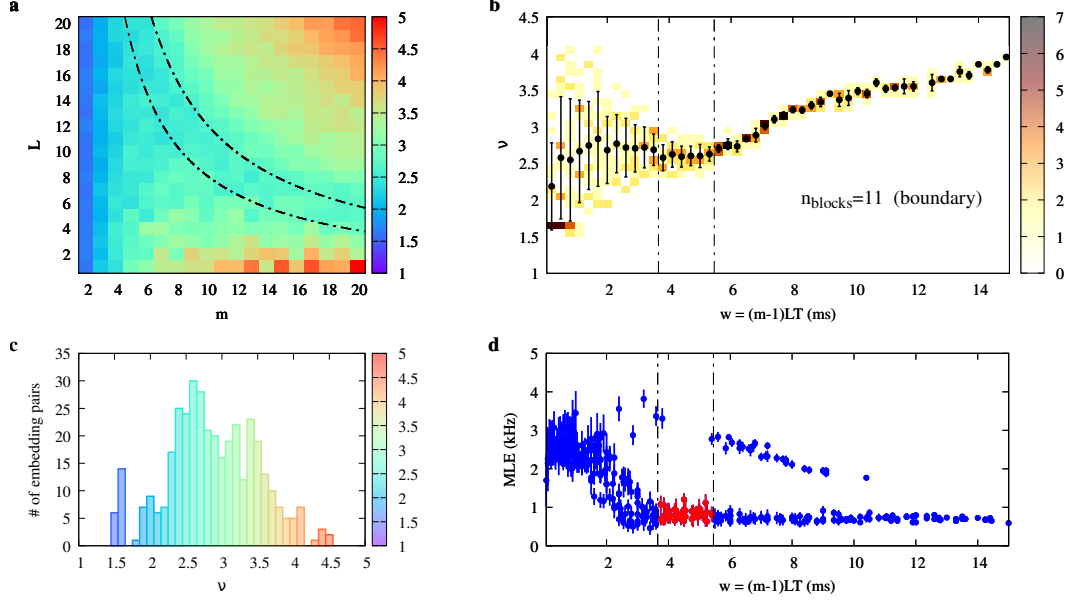


Figure B.10: “Chasing chaos” analysis of the experimental W_1 time series with 11 coupled blocks. (a) Map of estimated correlation dimension ν vs. embedding pair (m, L) . (b) Sample joint distribution of (w, ν) for the ν -map in (a). (c) Histogram of the estimated ν . (d) Distribution of MLE as a function of w .

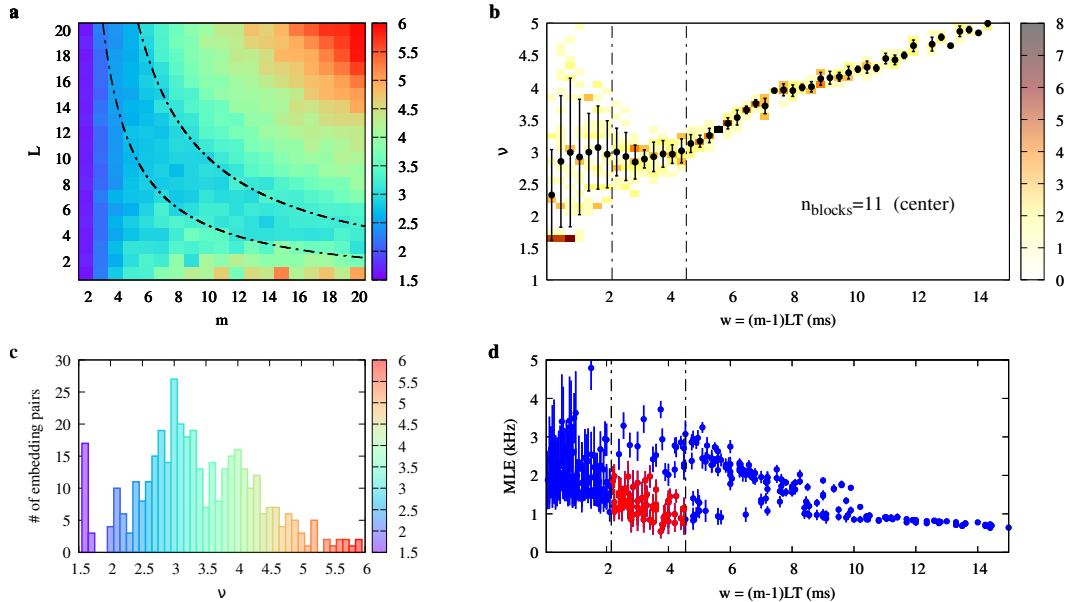


Figure B.11: “Chasing chaos” analysis of the experimental W_6 time series with 11 coupled blocks. (a) Map of estimated correlation dimension ν vs. embedding pair (m, L) . (b) Sample joint distribution of (w, ν) for the ν -map in (a). (c) Histogram of the estimated ν . (d) Distribution of MLE as a function of w .

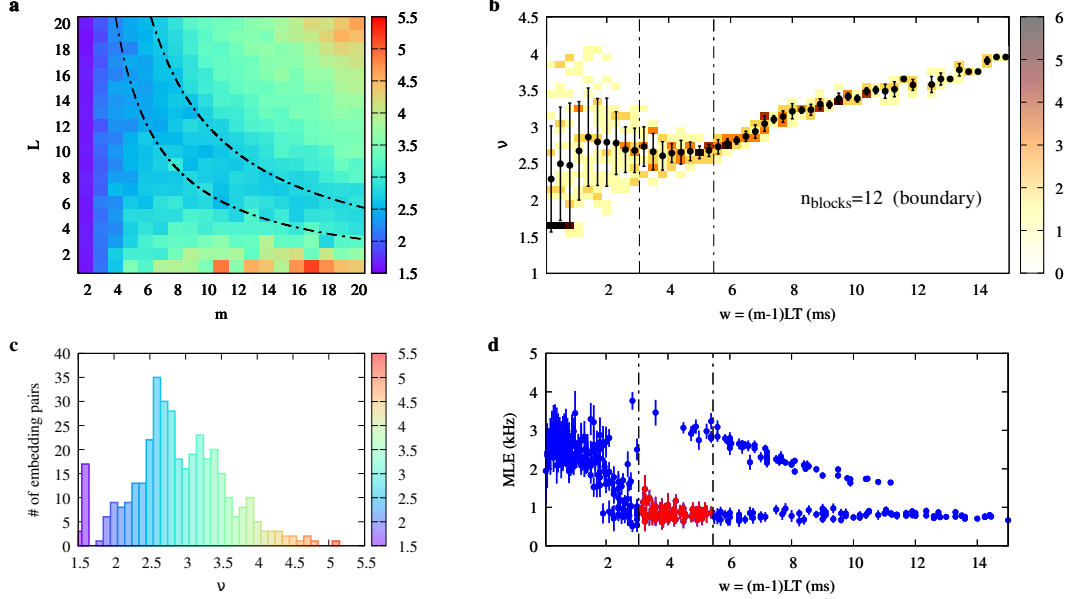


Figure B.12: “Chasing chaos” analysis of the experimental W_1 time series with 12 coupled blocks. (a) Map of estimated correlation dimension ν vs. embedding pair (m, L) . (b) Sample joint distribution of (w, ν) for the ν -map in (a). (c) Histogram of the estimated ν . (d) Distribution of MLE as a function of w .

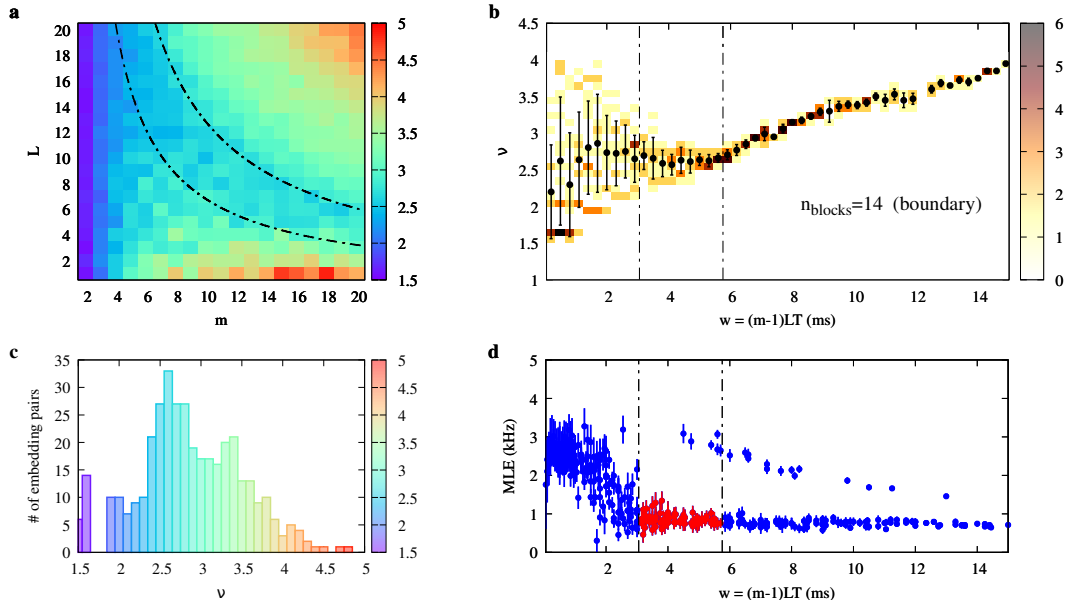


Figure B.13: “Chasing chaos” analysis of the experimental W_1 time series with 14 coupled blocks. (a) Map of estimated correlation dimension ν vs. embedding pair (m, L) . (b) Sample joint distribution of (w, ν) for the ν -map in (a). (c) Histogram of the estimated ν . (d) Distribution of MLE as a function of w .

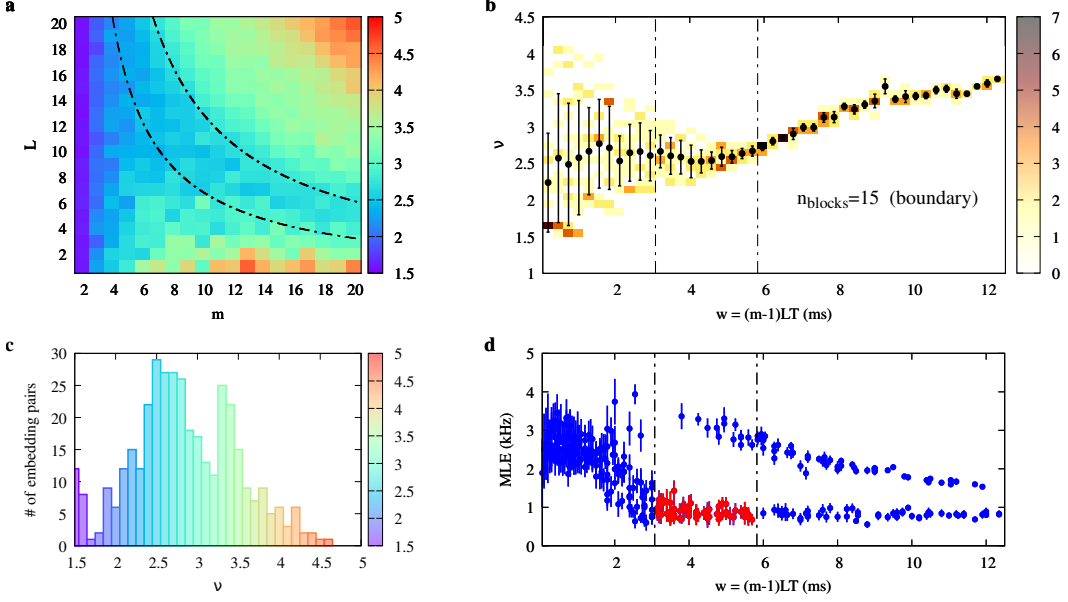


Figure B.14: “Chasing chaos” analysis of the experimental W_1 time series with 15 coupled blocks. (a) Map of estimated correlation dimension ν vs. embedding pair (m, L) . (b) Sample joint distribution of (w, ν) for the ν -map in (a). (c) Histogram of the estimated ν . (d) Distribution of MLE as a function of w .

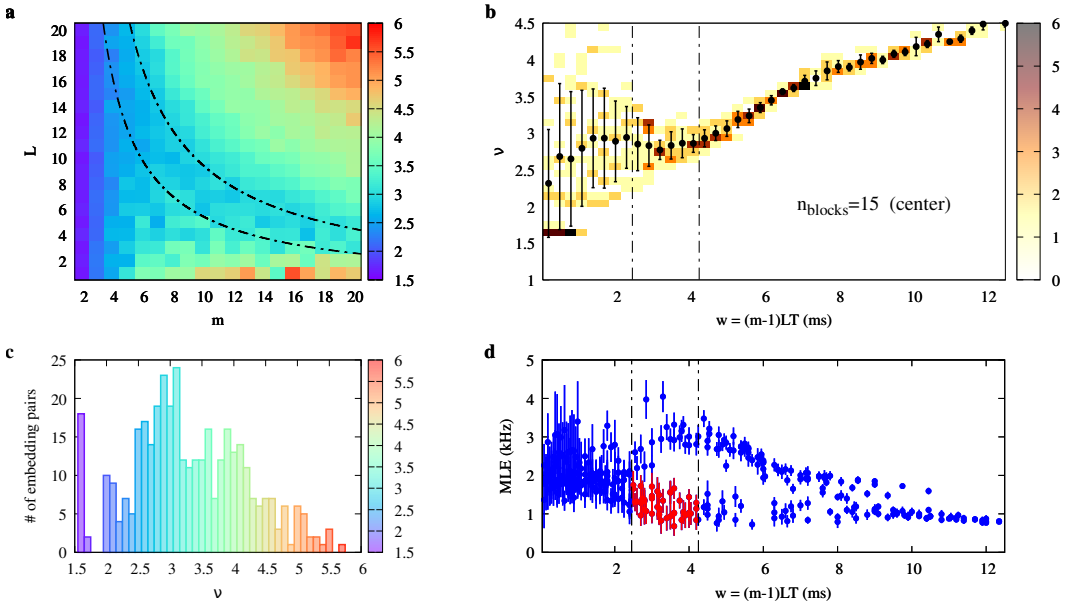


Figure B.15: “Chasing chaos” analysis of the experimental W_8 time series with 15 coupled blocks. (a) Map of estimated correlation dimension ν vs. embedding pair (m, L) . (b) Sample joint distribution of (w, ν) for the ν -map in (a). (c) Histogram of the estimated ν . (d) Distribution of MLE as a function of w .

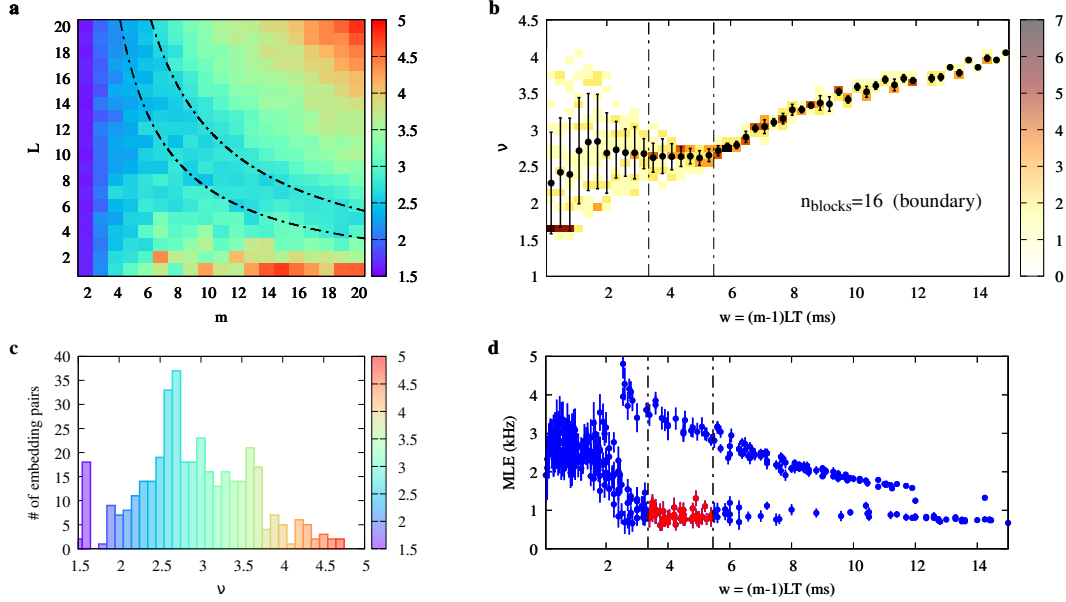


Figure B.16: “Chasing chaos” analysis of the experimental W_1 time series with 16 coupled blocks. (a) Map of estimated correlation dimension ν vs. embedding pair (m, L) . (b) Sample joint distribution of (w, ν) for the ν -map in (a). (c) Histogram of the estimated ν . (d) Distribution of MLE as a function of w .

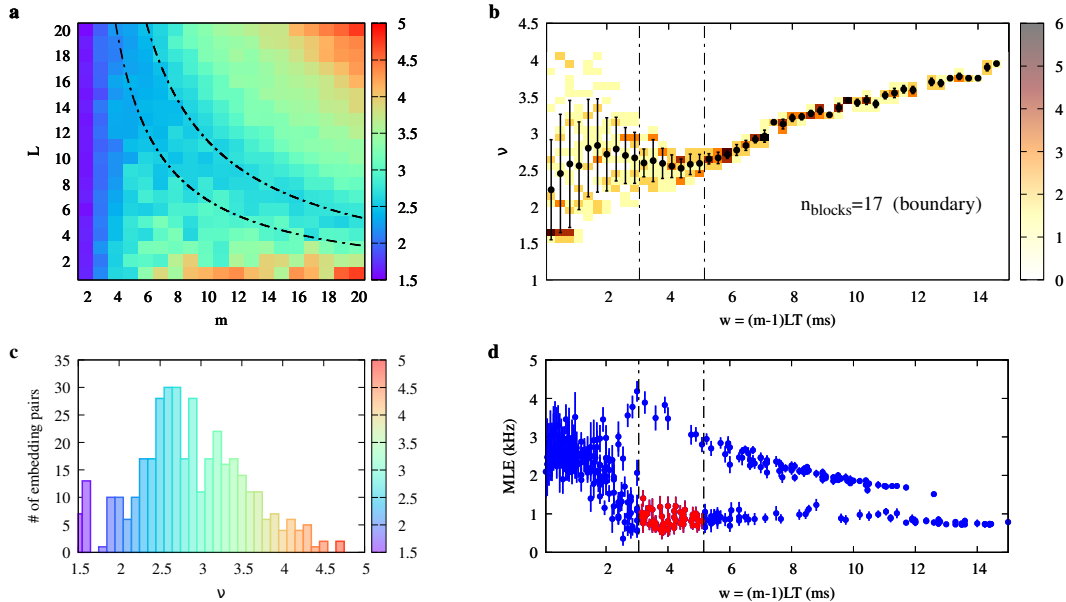


Figure B.17: “Chasing chaos” analysis of the experimental W_1 time series with 17 coupled blocks. (a) Map of estimated correlation dimension ν vs. embedding pair (m, L) . (b) Sample joint distribution of (w, ν) for the ν -map in (a). (c) Histogram of the estimated ν . (d) Distribution of MLE as a function of w .

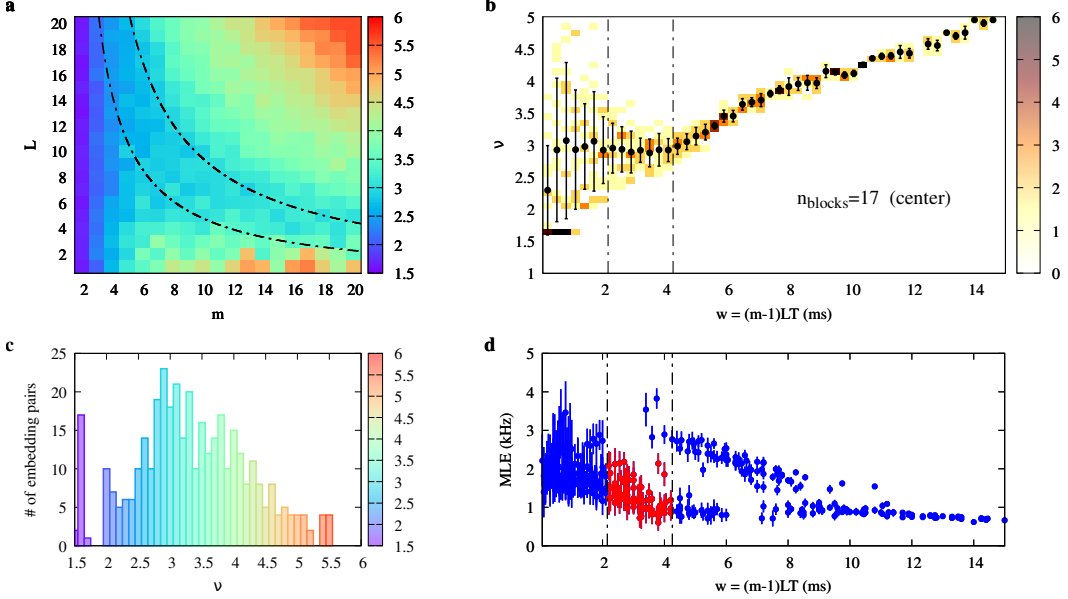


Figure B.18: “Chasing chaos” analysis of the experimental W_9 time series with 17 coupled blocks. (a) Map of estimated correlation dimension ν vs. embedding pair (m, L) . (b) Sample joint distribution of (w, ν) for the ν -map in (a). (c) Histogram of the estimated ν . (d) Distribution of MLE as a function of w .

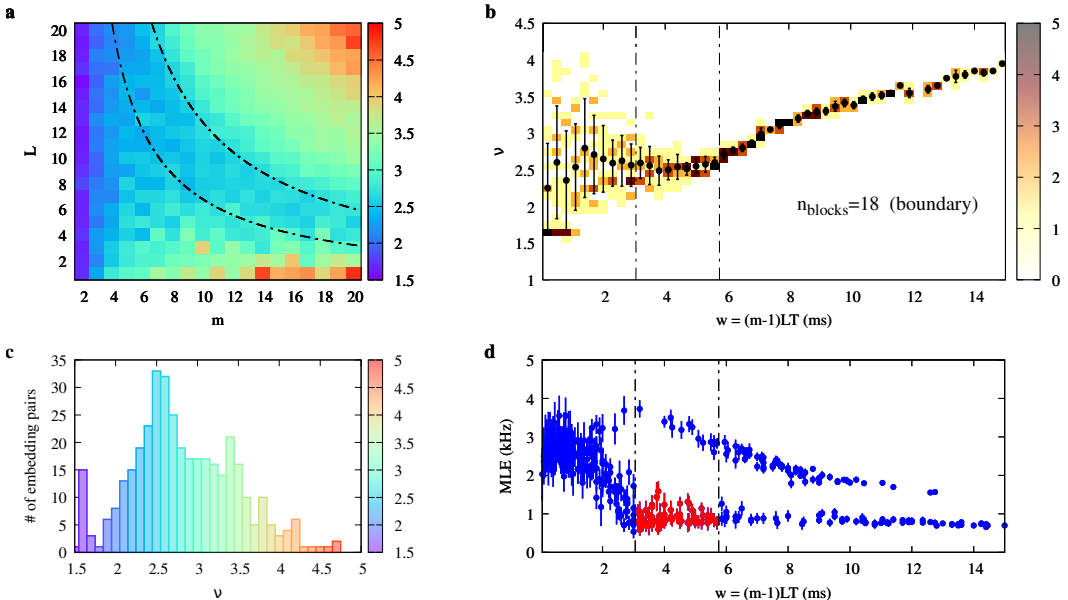


Figure B.19: “Chasing chaos” analysis of the experimental W_1 time series with 18 coupled blocks. (a) Map of estimated correlation dimension ν vs. embedding pair (m, L) . (b) Sample joint distribution of (w, ν) for the ν -map in (a). (c) Histogram of the estimated ν . (d) Distribution of MLE as a function of w .

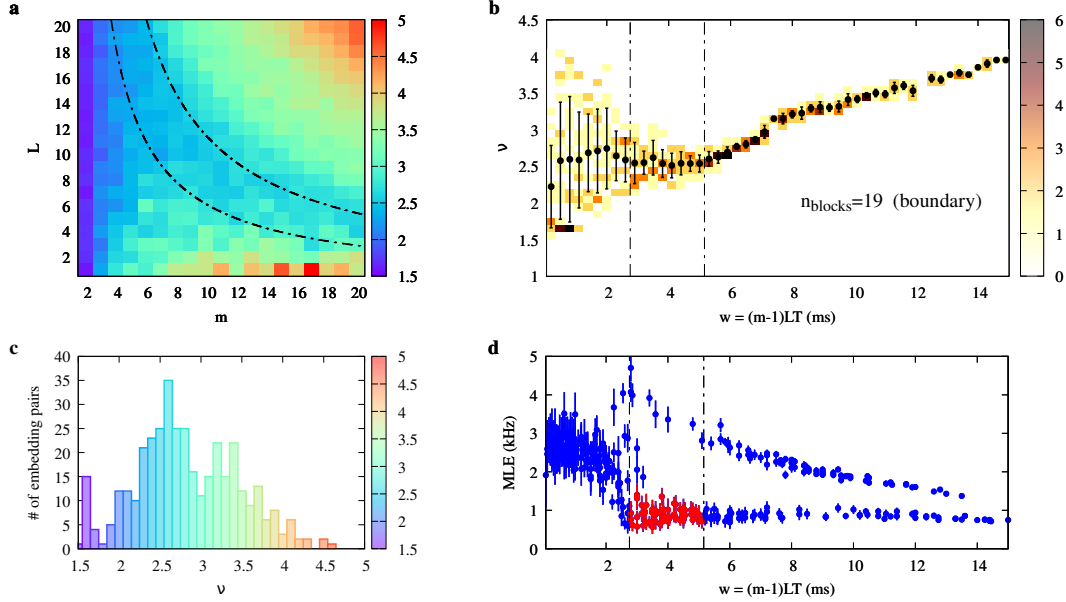


Figure B.20: “Chasing chaos” analysis of the experimental W_1 time series with 19 coupled blocks. (a) Map of estimated correlation dimension ν vs. embedding pair (m, L) . (b) Sample joint distribution of (w, ν) for the ν -map in (a). (c) Histogram of the estimated ν . (d) Distribution of MLE as a function of w .

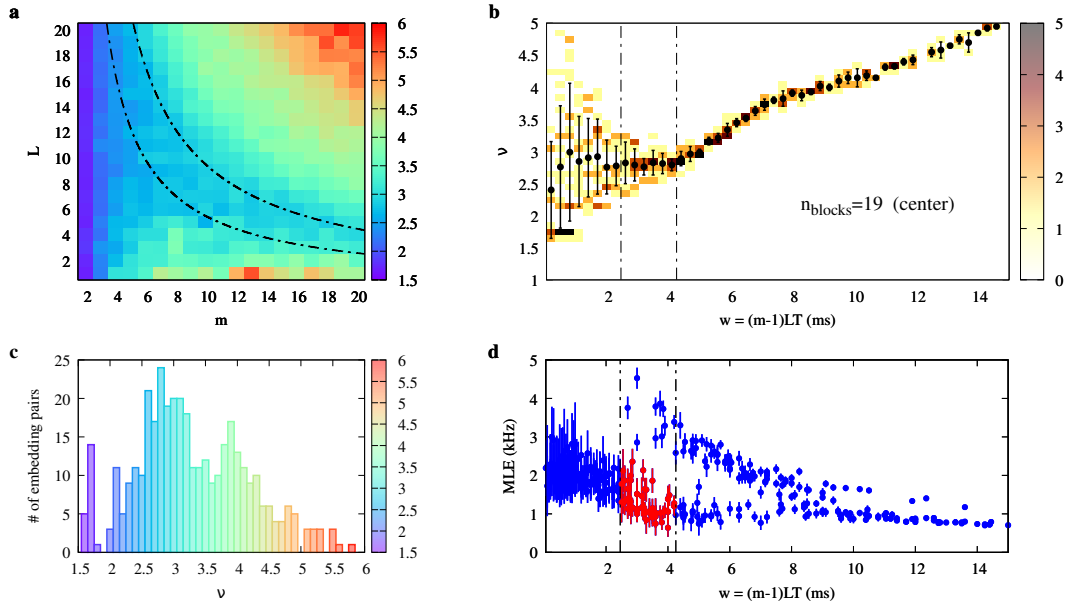


Figure B.21: “Chasing chaos” analysis of the experimental W_{10} time series with 19 coupled blocks. (a) Map of estimated correlation dimension ν vs. embedding pair (m, L) . (b) Sample joint distribution of (w, ν) for the ν -map in (a). (c) Histogram of the estimated ν . (d) Distribution of MLE as a function of w .

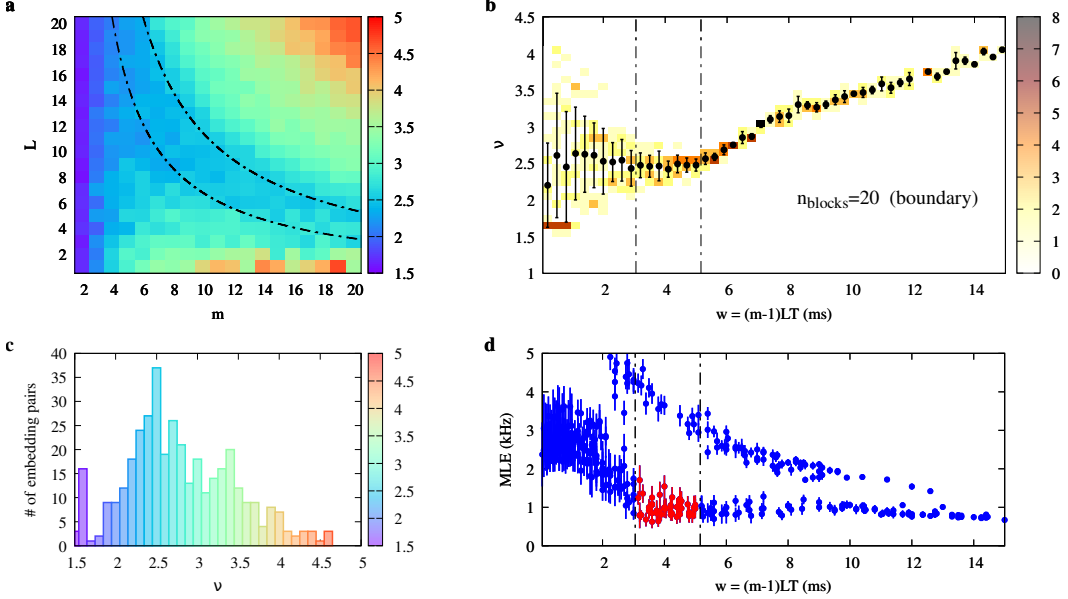


Figure B.22: “Chasing chaos” analysis of the experimental W_1 time series with 20 coupled blocks. (a) Map of estimated correlation dimension ν vs. embedding pair (m, L) . (b) Sample joint distribution of (w, ν) for the ν -map in (a). (c) Histogram of the estimated ν . (d) Distribution of MLE as a function of w .

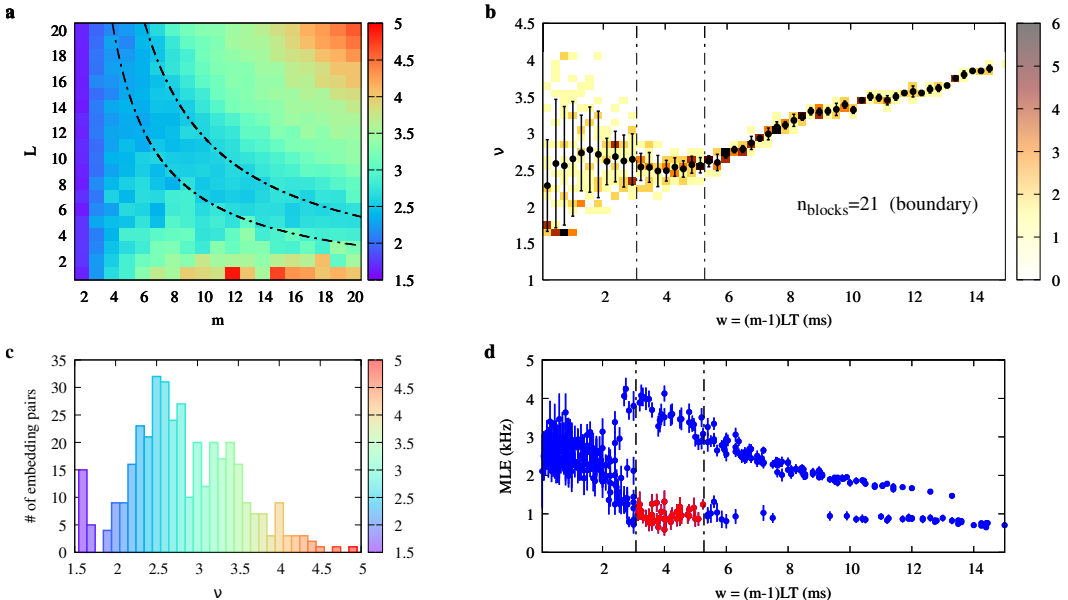


Figure B.23: “Chasing chaos” analysis of the experimental W_1 time series with 21 coupled blocks. (a) Map of estimated correlation dimension ν vs. embedding pair (m, L) . (b) Sample joint distribution of (w, ν) for the ν -map in (a). (c) Histogram of the estimated ν . (d) Distribution of MLE as a function of w .

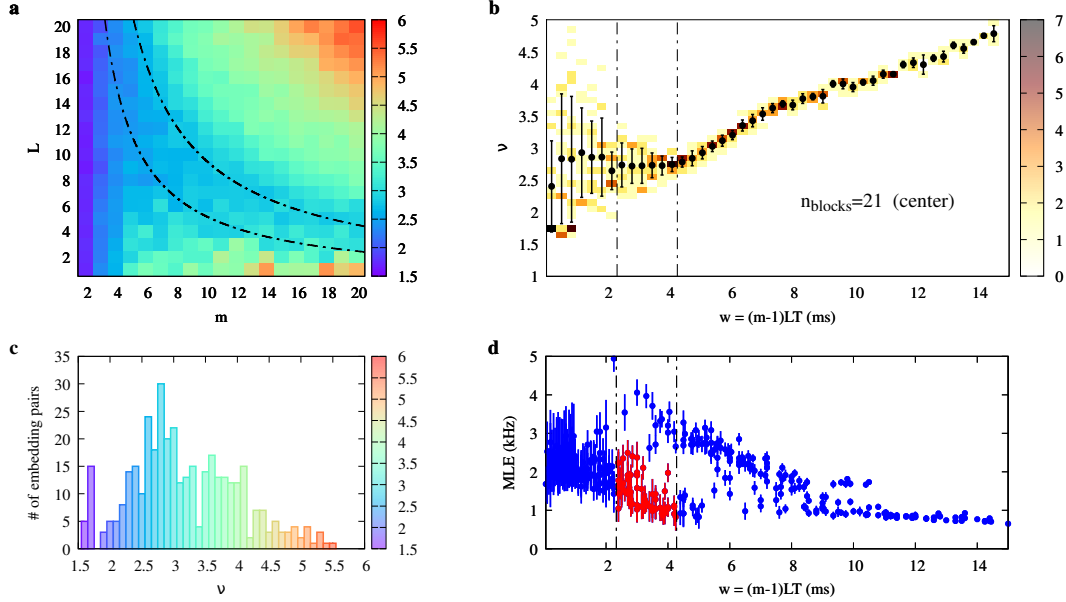


Figure B.24: “Chasing chaos” analysis of the experimental W_{11} time series with 21 coupled blocks. (a) Map of estimated correlation dimension ν vs. embedding pair (m, L) . (b) Sample joint distribution of (w, ν) for the ν -map in (a). (c) Histogram of the estimated ν . (d) Distribution of MLE as a function of w .

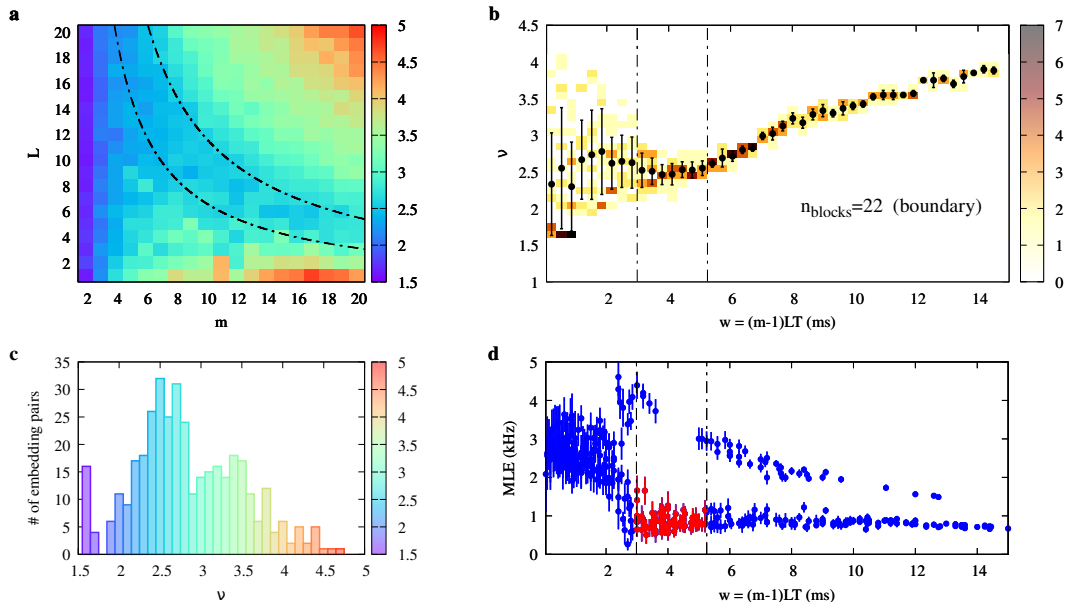


Figure B.25: “Chasing chaos” analysis of the experimental W_1 time series with 22 coupled blocks. (a) Map of estimated correlation dimension ν vs. embedding pair (m, L) . (b) Sample joint distribution of (w, ν) for the ν -map in (a). (c) Histogram of the estimated ν . (d) Distribution of MLE as a function of w .

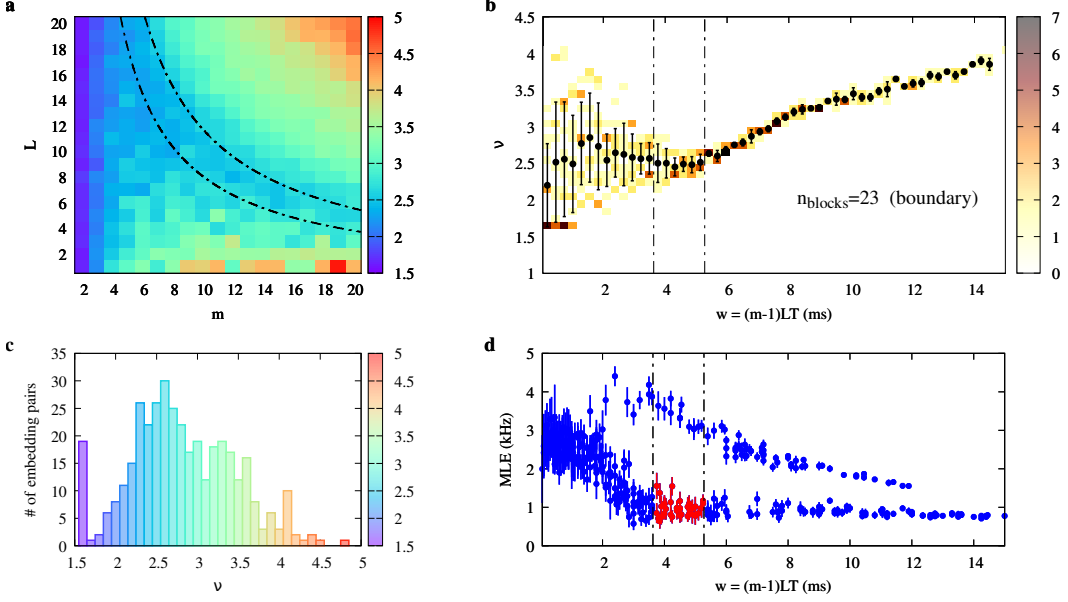


Figure B.26: “Chasing chaos” analysis of the experimental W_1 time series with 23 coupled blocks. (a) Map of estimated correlation dimension ν vs. embedding pair (m, L) . (b) Sample joint distribution of (w, ν) for the ν -map in (a). (c) Histogram of the estimated ν . (d) Distribution of MLE as a function of w .

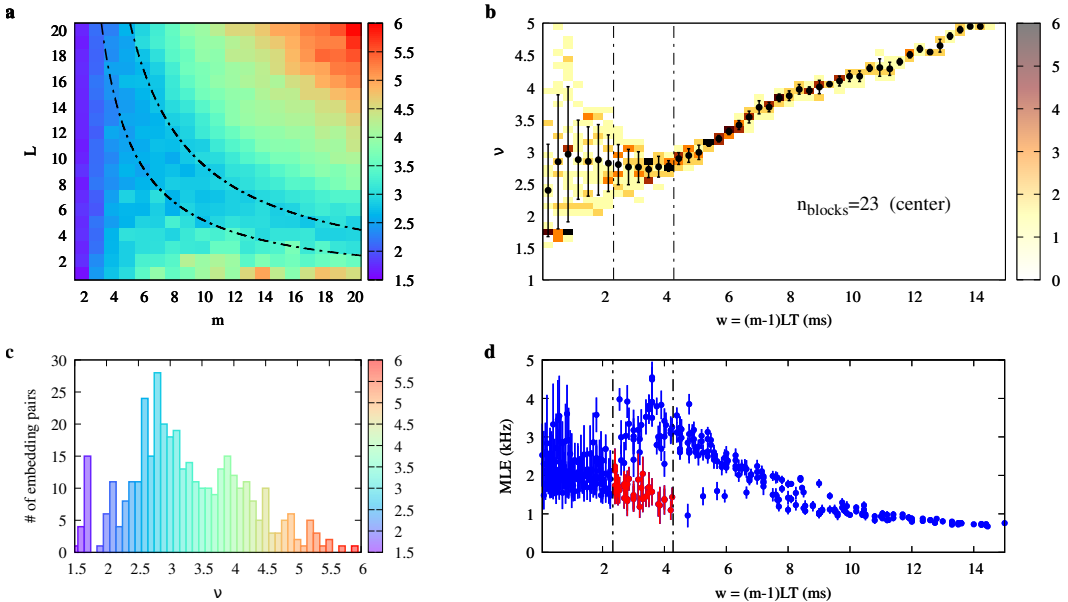


Figure B.27: “Chasing chaos” analysis of the experimental W_{12} time series with 23 coupled blocks. (a) Map of estimated correlation dimension ν vs. embedding pair (m, L) . (b) Sample joint distribution of (w, ν) for the ν -map in (a). (c) Histogram of the estimated ν . (d) Distribution of MLE as a function of w .

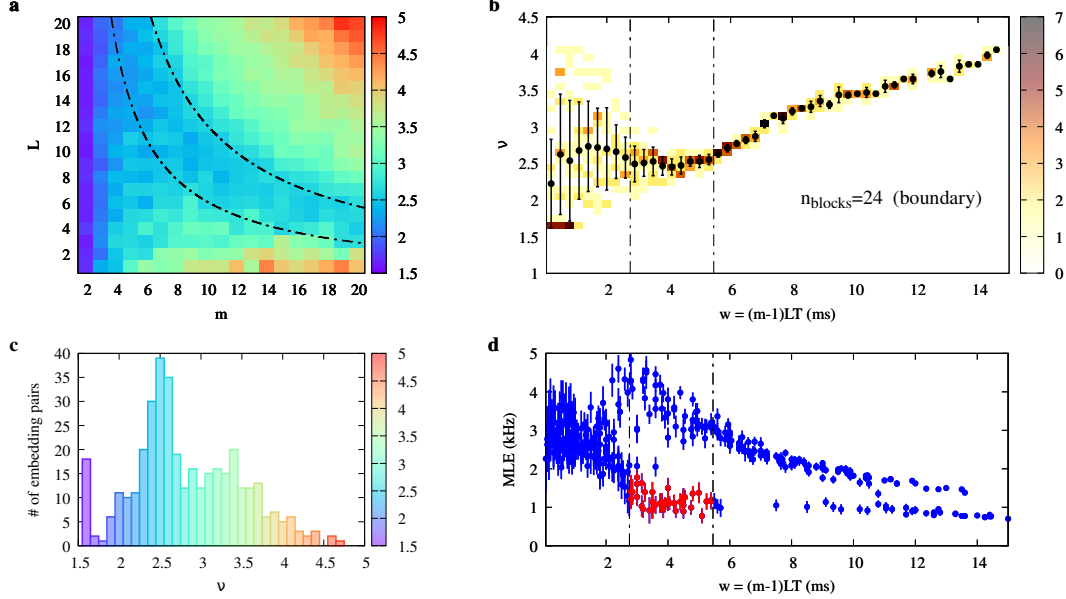


Figure B.28: “Chasing chaos” analysis of the experimental W_1 time series with 24 coupled blocks. (a) Map of estimated correlation dimension ν vs. embedding pair (m, L) . (b) Sample joint distribution of (w, ν) for the ν -map in (a). (c) Histogram of the estimated ν . (d) Distribution of MLE as a function of w .

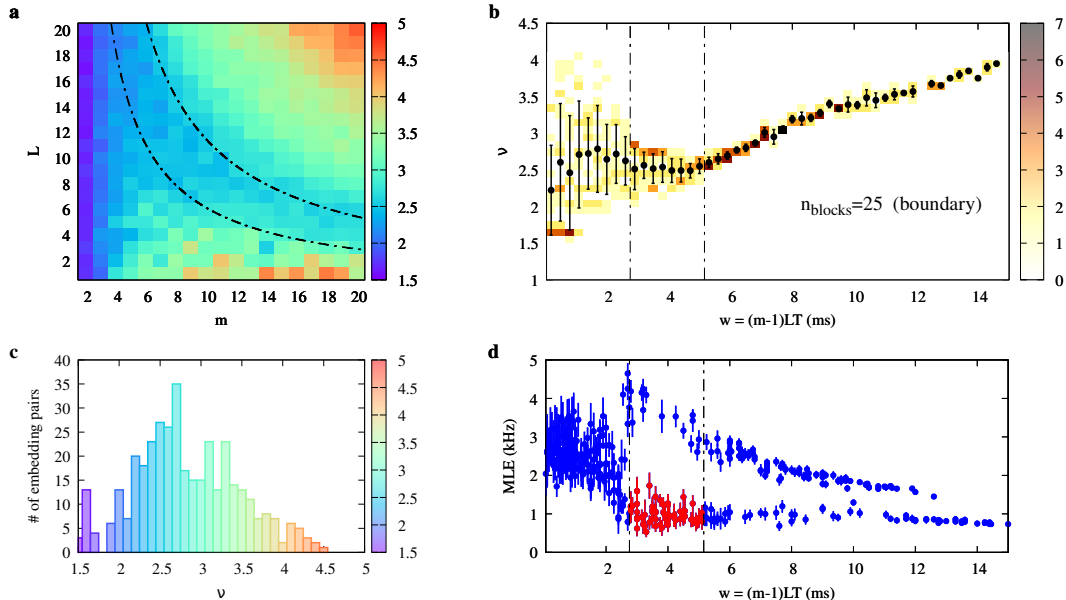


Figure B.29: “Chasing chaos” analysis of the experimental W_1 time series with 25 coupled blocks. (a) Map of estimated correlation dimension ν vs. embedding pair (m, L) . (b) Sample joint distribution of (w, ν) for the ν -map in (a). (c) Histogram of the estimated ν . (d) Distribution of MLE as a function of w .

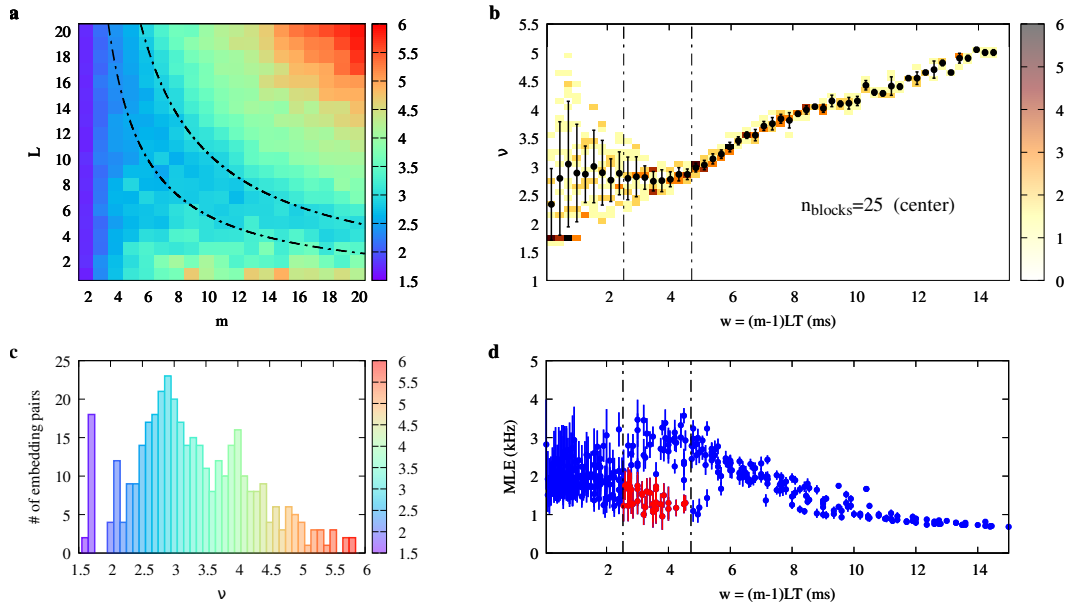


Figure B.30: “Chasing chaos” analysis of the experimental W_{13} time series with 25 coupled blocks. (a) Map of estimated correlation dimension ν vs. embedding pair (m, L) . (b) Sample joint distribution of (w, ν) for the ν -map in (a). (c) Histogram of the estimated ν . (d) Distribution of MLE as a function of w .

Bibliography

- [1] Beno Gutenberg. “The energy of earthquakes”. In: *Quarterly Journal of the Geological Society* 112.1-4 (1956), pp. 1–14.
- [2] Robert Burridge and Leon Knopoff. “Model and theoretical seismicity”. In: *Bulletin of the seismological society of america* 57.3 (1967), pp. 341–371.
- [3] Zeev Olami, Hans Jacob S. Feder, and Kim Christensen. “Self-organized criticality in a continuous, nonconservative cellular automaton modeling earthquakes”. In: *Physical review letters* 68.8 (1992), p. 1244.
- [4] Alessio Perinelli, Roberto Iuppa, and Leonardo Ricci. “A scalable electronic analog of the Burridge–Knopoff model of earthquake faults”. In: *Chaos: An Interdisciplinary Journal of Nonlinear Science* 33.9 (2023).
- [5] Stuart Field, Naia Venturi, and Franco Nori. “Marginal stability and chaos in coupled faults modeled by nonlinear circuits”. In: *Physical review letters* 74.1 (1995), p. 74.
- [6] Karl Popp and Peter Stelter. “Stick-slip vibrations and chaos”. In: *Philosophical Transactions: Physical Sciences and Engineering* (1990), pp. 89–105.
- [7] James Theiler. “Estimating fractal dimension”. In: *JOSA a* 7.6 (1990), pp. 1055–1073.
- [8] Robert Devaney. *An introduction to chaotic dynamical systems*. CRC press, 2018.
- [9] Edward Ott. *Chaos in dynamical systems*. Cambridge university press, 2002.
- [10] Benoit B. Mandelbrot. “Is nature fractal?” In: *Science* 279.5352 (1998), p. 783.
- [11] Edward N. Lorenz. “Deterministic nonperiodic flow”. In: *Journal of atmospheric sciences* 20.2 (1963), pp. 130–141.
- [12] Henry D.I. Abarbanel et al. “The analysis of observed chaotic data in physical systems”. In: *Reviews of modern physics* 65.4 (1993), p. 1331.
- [13] Celso Grebogi et al. “Strange attractors that are not chaotic”. In: *Physica D: Nonlinear Phenomena* 13.1-2 (1984), pp. 261–268.
- [14] Michel Hénon. “A two-dimensional mapping with a strange attractor”. In: *The theory of chaotic attractors* (2004), pp. 94–102.
- [15] Ivar Bendixson. “Sur les courbes définies par des équations différentielles”. In: *Acta Mathematica* 24 (1901).

- [16] Norman H. Packard et al. “Geometry from a time series”. In: *Physical review letters* 45.9 (1980), p. 712.
- [17] Elizabeth Bradley and Holger Kantz. “Nonlinear time-series analysis revisited”. In: *Chaos: An Interdisciplinary Journal of Nonlinear Science* 25.9 (2015).
- [18] Otto E. Rössler. “Continuous chaos”. In: *Synergetics: A Workshop Proceedings of the International Workshop on Synergetics at Schloss Elmau, Bavaria, May 2–7, 1977*. Springer. 1977, pp. 184–197.
- [19] Floris Takens. “Detecting strange attractors in turbulence”. In: *Dynamical Systems and Turbulence, Warwick 1980: proceedings of a symposium held at the University of Warwick 1979/80*. Springer. 2006, pp. 366–381.
- [20] Ricardo Mañé. “On the dimension of the compact invariant sets of certain non-linear maps”. In: *Dynamical Systems and Turbulence, Warwick 1980: Proceedings of a Symposium Held at the University of Warwick 1979/80*. Springer. 2006, pp. 230–242.
- [21] Mingzhou Ding et al. “Estimating correlation dimension from a chaotic time series: when does plateau onset occur?” In: *Physica D: Nonlinear Phenomena* 69.3-4 (1993), pp. 404–424.
- [22] Peter Grassberger, Thomas Schreiber, and Carsten Schaffrath. “Nonlinear time sequence analysis”. In: *International Journal of Bifurcation and Chaos* 1.03 (1991), pp. 521–547.
- [23] Alessio Perinelli and Leonardo Ricci. “Identification of suitable embedding dimensions and lags for time series generated by chaotic, finite-dimensional systems”. In: *Physical Review E* 98.5 (2018), p. 052226.
- [24] Alessio Perinelli and Leonardo Ricci. “Chasing chaos by improved identification of suitable embedding dimensions and lags”. In: *Chaos: An Interdisciplinary Journal of Nonlinear Science* 30.12 (2020).
- [25] Martin Casdagli et al. “State space reconstruction in the presence of noise”. In: *Physica D: Nonlinear Phenomena* 51.1-3 (1991), pp. 52–98.
- [26] Alan Wolf et al. “Quantifying chaos with Lyapunov exponents”. In: *Chaos* 16 (1986), pp. 285–317.
- [27] Jianbo Gao and Zhemin Zheng. “Local exponential divergence plot and optimal embedding of a chaotic time series”. In: *Physics Letters A* 181.2 (1993), pp. 153–158.
- [28] Matteo Franchi and Leonardo Ricci. “Statistical properties of the maximum Lyapunov exponent calculated via the divergence rate method”. In: *Physical Review E* 90.6 (2014), p. 062920.
- [29] Leonardo Ricci, Alessio Perinelli, and Matteo Franchi. “Asymptotic behavior of the time-dependent divergence exponent”. In: *Physical Review E* 101.4 (2020), p. 042211.

- [30] James Theiler. “Spurious dimension from correlation algorithms applied to limited time-series data”. In: *Physical review A* 34.3 (1986), p. 2427.
- [31] Alfonso M. Albano, P.E. Rapp, and A. Passamante. “Kolmogorov-Smirnov test distinguishes attractors with similar dimensions”. In: *Physical Review E* 52.1 (1995), p. 196.
- [32] H.S. Greenside et al. “Impracticality of a box-counting algorithm for calculating the dimensionality of strange attractors”. In: *Physical Review A* 25.6 (1982), p. 3453.
- [33] Peter Grassberger and Itamar Procaccia. “Measuring the strangeness of strange attractors”. In: *Physica D: nonlinear phenomena* 9.1-2 (1983), pp. 189–208.
- [34] A.R. Osborne and A. Provenzale. “Finite correlation dimension for stochastic systems with power-law spectra”. In: *Physica D: Nonlinear Phenomena* 35.3 (1989), pp. 357–381.
- [35] John R. Dormand and Peter J. Prince. “Runge-kutta triples”. In: *Computers & Mathematics with Applications* 12.9 (1986), pp. 1007–1017.
- [36] Julien Clinton Sprott and George Rowlands. “Improved correlation dimension calculation”. In: *International Journal of Bifurcation and Chaos* 11.07 (2001), pp. 1865–1880.
- [37] Giancarlo Benettin et al. “Lyapunov characteristic exponents for smooth dynamical systems and for Hamiltonian systems; a method for computing all of them. Part 1: Theory”. In: *Meccanica* 15 (1980), pp. 9–20.
- [38] Giancarlo Benettin et al. “Lyapunov characteristic exponents for smooth dynamical systems; a method for computing all of them. Part 2: Numerical application”. In: *Meccanica* 15 (1980), pp. 21–30.